



Draft Manuscript for Review

**Compositional and thermodynamic variability in a stratified magma chamber: Evidence from the Green Tuff Ignimbrite (Pantelleria, Italy)**

Journal:	<i>Journal of Petrology</i>
Manuscript ID	JPET-Mar-18-0028.R1
Manuscript Type:	Original Manuscript
Date Submitted by the Author:	n/a
Complete List of Authors:	Liszewska, Katarzyna; University of Warsaw, IGMiP Faculty of Geology White, John; Eastern Kentucky University, Geography & Geology; Macdonald, Raymond; Lancaster University, Environment Centre; University of Warsaw, IGMiP Faculty of Geology Bagiński, Bogusław; University of Warsaw, IGMiP Faculty of Geology
Keyword:	Green Tuff ignimbrite, Pantelleria, zoned magma reservoir, magma mixing

SCHOLARONE™  
Manuscripts

# 1 Compositional and thermodynamic variability in a stratified magma 2 chamber: Evidence from the Green Tuff Ignimbrite (Pantelleria, Italy)

3 K.M. Liszewska<sup>1</sup>, J.C. White<sup>2</sup>, R. Macdonald<sup>1,3,\*</sup> and B. Bagiński<sup>1</sup>

4 <sup>1</sup>IGMiP Faculty of Geology, University of Warsaw, al. Żwirki i Wigury 93, 02-089 Warsaw, Poland

5 <sup>2</sup>Department of Geosciences, Eastern Kentucky University, Richmond, KY 40475, USA

6 <sup>3</sup>Environment Centre, Lancaster University, Lancaster LA1 4YQ, UK

7 \*Corresponding author. e-mail; [r.macdonald@lancaster.ac.uk](mailto:r.macdonald@lancaster.ac.uk). Telephone 0048 22772 4953

## 8 9 ABSTRACT

10 The Green Tuff Ignimbrite, Pantelleria, is compositionally zoned from pantellerite at the base to comenditic  
11 trachyte at the top, the variation **apparently** representing an inverted vertical zonation in the pre-eruptive  
12 reservoir. The main phenocryst assemblages are alkali feldspar + olivine + clinopyroxene + ilmenite + apatite in  
13 the trachytes and alkali feldspar + aenigmatite + clinopyroxene ± quartz in the rhyolites. Thermodynamic  
14 modelling indicates that the temperature range was ~900-700°C,  $f_{O_2}$  FMQ-1.5 to FMQ-0.5 and  $a_{SiO_2}$  (relative to  
15 quartz saturation) 0.74-1.00. **Melt water contents ranged from ~1 wt % in the trachytes to ~4 wt % in the**  
16 **pantellerites.** Matrix glass analyses in the more evolved rocks are highly variable, showing that compositional  
17 layers in the upper parts of the reservoir, formed by fractional crystallization, were mixed during eruption, the  
18 proportion of rhyolitic to trachytic melts increasing towards the top of the reservoir. Some areas of glass have  
19 low Al<sub>2</sub>O<sub>3</sub> contents (5.16-5.46 wt %) and high FeO\* contents (9.66-10.02 wt %), making them the most evolved  
20 melts yet reported from Pantelleria. **The new glass data stress how whole-rock analyses do not truly reflect the**  
21 **complete range of melt compositions in the pre-eruptive reservoir. The trachytes contain >40% modal**  
22 **phenocrysts, which with relatively high Ba contents and positive Eu anomalies, are considered to have originated**  
23 **in a feldspar-accumulitic layer. Phenocrysts in the trachytes are commonly heavily resorbed, inferred to be a**  
24 **result of heating by influxes of intermediate composition magmas, which, however, were not erupted. It is**  
25 **argued that magma of intermediate composition were present in the Green Tuff reservoir but were efficiently**  
26 **trapped in a crystal-rich layer below the Green Tuff magmas, which was eventually erupted during a resurgent**  
27 **phase as the Montagna Grande Trachyte.**

28 **Key words:** Green Tuff ignimbrite; Pantelleria; zoned magma reservoir; magma mixing

29  
30  
31  
32  
33  
34  
35  
36  
37  
38  
39  
40  
41  
42  
43  
44  
45  
46  
47  
48  
49  
50  
51  
52  
53  
54  
55  
56  
57  
58  
59  
60

## 30 INTRODUCTION

31 The island of Pantelleria, located in the Strait of Sicily continental rift system, is a composite,  
32 bimodal volcano, with alkali basalt and peralkaline rhyolite end-members. Rocks of  
33 intermediate composition, such as mugearites and benmoreites, are rare and in many, perhaps  
34 all, cases are **products of magma mixing** (Ferla & Meli, 2006; Romengo *et al.*, 2012). Despite  
35 intensive study since the 1960s, **some** aspects of the evolution of Pantelleria remain  
36 enigmatic, including (i) the location and nature of the magma reservoir(s), (ii) the genetic  
37 relationships between the mafic and silicic volcanic rocks, and (iii) the detailed changes in  
38 crystallization conditions during magma evolution. The deposit termed the Green Tuff is an  
39 important focus in addressing these, and related, problems.

40 (a) The Green Tuff is compositionally zoned from **pantellerite to trachyte**, which has been  
41 inferred to represent vertical compositional variation within the pre-eruptive magma chamber,  
42 **with the pantellerites being erupted first**. The zonation allows us to examine the genetic  
43 relationships between them in the products of one eruption, using whole-rock, matrix glass  
44 and mineral chemical data.

45 (b) The trachytic members show strong textural disequilibrium, which must be related to  
46 processes in the lower part of the erupted magma reservoir, such as thermal and/or  
47 compositional inputs from more mafic melts *via* magma mixing. This, in turn, can provide  
48 evidence on the material in the sub-trachyte part of the chamber and thus on the existence or  
49 otherwise of a composition (Daly) gap in the plumbing system.

50 (c) The phenocryst assemblages are suitable for estimating such parameters as temperature,  
51  $fO_2$  and  $aSiO_2$ , how they varied with melt composition and inferred depth in the magma  
52 chamber prior to eruption and the evidence they provide for a volatile gradient.

53

54 **GEOLOGICAL SETTING**

55 Pantelleria is located in the NW-SE trending Strait of Sicily Rift Zone (Fig. 1). The rift cuts  
56 the Pelagian Block, a promontory of the African plate. The crustal thickness under most of the  
57 Block is 25-35 km, thinning to 16-17 km in the rift zone (Civile *et al.*, 2008). The Pantelleria  
58 Trough is one of three basins within the rift; **it is a deep trough with a bathymetric low**  
59 **reaching a depth of -1317 m (Morelli *et al.*, 1975).** The trough has a strong positive Bouguer  
60 anomaly (65-103 mgal; Behncke *et al.* 2006; Civile *et al.*, 2008). **It also has a high average**  
61 **heat flow ( $94 \pm 21$  mW/m<sup>2</sup>; Verzhbitsky & Kononov, 2003), which contrasts with the**  
62 **continental average of 55 mW/m<sup>2</sup> but is in line with the fact that southern Italy is a hot spot in**  
63 **Europe, with an average of 70 mW/m<sup>2</sup> (Chapman & Pollack, 1975). These features have been**  
64 **taken to indicate the presence of abundant basaltic magmas at depth (Della Vedova *et al.*,**  
65 **1995) and asthenospheric upwelling to ~60 km, which is coincident with the maximum depth**  
66 **of earthquake foci that have been recorded in this area (Calò and Parisi, 2014). Little is known**  
67 of the composition of the submerged part of Pantelleria. Geophysical work by Gantar *et al.*  
68 (1961) showed that it comprises a large volume of high density rocks (3000 kg/m<sup>3</sup>). By  
69 analogy with Linosa, a volcanic island some 100 km SE of Pantelleria in the Strait of Sicily,  
70 the rocks may be dominated by basalts and hawaiites (Villari, 1974). The most recent,  
71 basaltic, eruption in the area was submarine and occurred a few kilometres to the NW of the  
72 island in 1891.

73 At the current level of exposure, Pantelleria is dominated (**~94%; Mahood & Stimac, 1986**)  
74 by trachytes and rhyolites. Eruption of basalts and hawaiites has been restricted to the  
75 northern part of the island. Furthermore, a well (PPT2) drilled in the northern section  
76 penetrated, at 180 m depth, more than 600 m of basaltic lavas and hyaloclastites cut by

3

1  
2  
3 77 dolerite dykes (Fulignati *et al.*, 1997). A basaltic component has been recognized in mixed  
4  
5 78 magma rocks from various centres on the island, indicating the continuing presence of mafic  
6  
7 79 magma at depth (Ferla & Meli, 2006; Romengo *et al.*, 2012). Magmatic activity at Pantelleria  
8  
9 80 is undoubtedly basalt-driven, in that basaltic magma is the fundamental source of mass, heat  
10  
11 81 and volatiles in the system.

12  
13  
14 82 The Green Tuff forms a thin cover over much of the 83 km<sup>2</sup> island, draping all topographic  
15  
16 83 landforms (Fig. 1). High-precision <sup>40</sup>Ar/<sup>39</sup>Ar dating has given an eruption age of 45.7 ± 1.0 ka  
17  
18 84 (2σ) (Scaillet *et al.*, 2013). The volume (in DRE: dense rock equivalent) has been variously  
19  
20 85 estimated as 0.28 km<sup>3</sup> (Jordan *et al.*, 2018), 1.5 km<sup>3</sup> (Civetta *et al.*, 1988), 3.5 km<sup>3</sup> (Mahood  
21  
22 86 & Hildreth, 1986) and 7 km<sup>3</sup> (Wolff & Wright, 1981). The range partly reflects uncertainty in  
23  
24 87 the amount of material that fell into the sea: distal ash from the eruption has been identified as  
25  
26 88 far away as the Dodecanese, 1300 km east of Pantelleria (Margari *et al.*, 2007). Taking into  
27  
28 89 account the offshore deposit, Margari *et al.* (2007) suggested a bulk ash volume of ~10 km<sup>3</sup>  
29  
30 90 DRE. The range also reflects the very variable thickness of the Green Tuff, from 30 cm to  
31  
32 91 >10 m in palaeovalleys (Orsi & Sheridan, 1984). The deposit has been variously interpreted  
33  
34 92 as a welded ignimbrite (Villari, 1974), a welded fall deposit (Wolff & Wright, 1981) and a  
35  
36 93 sequence of pyroclastic flow units including welded fall and surge members (Orsi &  
37  
38 94 Sheridan, 1984). Mahood & Hildreth (1986) described the Green Tuff as a Plinian deposit,  
39  
40 95 commencing with fallout beds followed by pyroclastic flows. In the fullest, most recent study  
41  
42 96 Williams *et al.* (2014) interpreted the Green Tuff as a Plinian fall deposit overlain by a single  
43  
44 97 ignimbrite flow unit.

45  
46  
47  
48  
49 98 The location and nature of the eruptive sources of the Green Tuff are debatable. Following  
50  
51 99 Mahood & Hildreth (1986), it has generally been accepted that eruption of the Green Tuff at  
52  
53 100 45.7 ± 1.0 ka was related to the formation of the Cinque Denti caldera (~30 km<sup>2</sup>), the younger

1  
2  
3 101 of the two calderas on the island (Fig. 1). Wright (1980) argued for a central vent on the  
4  
5 102 western side of the Cinque Denti caldera, whereas Mahood & Hildreth (1986) located the vent  
6  
7 103 at the southern end of the caldera or in the Monte Gibeles area. Williams *et al.* (2014)  
8  
9 104 suggested that the vent was on the northwestern slope of Montagna Grande. In contrast,  
10  
11 105 Catalano *et al.* (2014) proposed that the tuff was erupted from fissures superimposed on NNE-  
12  
13 106 trending normal fault zones within the caldera complex. They further proposed that the  
14  
15 107 eruption caused only a partial collapse of the southeastern walls of the caldera, the main part  
16  
17 108 of which had formed earlier, perhaps at ~87 ka. Most recently, Jordan *et al.* (2018) have  
18  
19 109 argued that there have been five, or more, periods of caldera collapse on Pantelleria and that  
20  
21 110 the eruption of the Green Tuff was accompanied by only partial collapse along previously  
22  
23 111 established faults.

24  
25  
26  
27 112 The Green Tuff is continuously zoned from comenditic trachyte at the top to pantellerite at  
28  
29 113 the bottom, **reflecting in reverse order the eruption** from a zoned magma chamber (Mahood,  
30  
31 114 1984; Civetta *et al.*, 1988; Mahood & Hildreth, 1986; Williams *et al.*, 2014). **Judging from the**  
32  
33 115 **stratigraphic height versus composition profile in Williams *et al.* (2014), the trachyte forms an**  
34  
35 116 **estimated 5-10% of the deposit.** An important aspect of the Green Tuff, in terms of the  
36  
37 117 evolution of Pantelleria, is that its eruption marked a peak in melt production and in the  
38  
39 118 peralkalinity of the magmas, after a long inter-eruptive period following the 85 ka eruptive  
40  
41 119 episode (Mahood & Hildreth, 1986; Scaillet *et al.*, 2013). On the basis of new  $^{40}\text{Ar}/^{39}\text{Ar}$   
42  
43 120 dating and geodetic evidence of deflation and subsidence of the caldera floor, Scaillet *et al.*  
44  
45 121 (2011) proposed that the intracaldera system, in stasis since 7 ka, is on the wane and that there  
46  
47 122 is no evidence of a forthcoming eruption.

48  
49  
50  
51 123 Formation of the Green Tuff was followed by eruption onto the caldera floor of the  
52  
53 124 volcanic rocks forming Monte Gibeles (44-37 ka), which was subsequently uplifted as a

1  
2  
3 125 resurgent block and then tilted to form Montagna Grande at ~18 ka (Fig. 1) (Mahood &  
4  
5 126 Hildreth, 1986; Orsi *et al.*, 1991; Lanzo *et al.*, 2013). This edifice is composed dominantly of  
6  
7 127 metaluminous trachytes, with a single recorded example of benmoreite lava (Romengo *et al.*,  
8  
9 128 2012). K-Ar dates for the trachytes overlap those of the Green Tuff, prompting Mahood &  
10  
11 129 Hildreth (1986) to suggest that the trachytic activity was a continuation of the Green Tuff  
12  
13 130 activity, i.e. it was probably part of the same magmatic system, where continuing eruptions  
14  
15 131 were a response to isostatic compensation for the material ejected during caldera formation. In  
16  
17 132 contrast, Civetta *et al.* (1988) considered the Green Tuff activity to be a late-stage part of the  
18  
19 133 earliest of six eruptive cycles on Pantelleria, whereas Montagna Grande was the earliest part  
20  
21 134 of a second cycle. However, the existence of the six cycles has been questioned by Scaillet *et*  
22  
23 135 *al.* (2011), partly on the basis of newer, high precision  $^{40}\text{Ar}/^{39}\text{Ar}$  ages. In the activity of the  
24  
25 136 past 20 ka, they recognized a long-term (>15 ka) decline in eruptive frequency associated with  
26  
27 137 a prominent palaeosol horizon marking a volcanic hiatus between 12 and 14 ka.  
28  
29  
30

31 138 Using the joint inversion of geodetic data (levelling, EDM and InSAR), Mattia *et al.* (2007)  
32  
33 139 found that the main caldera is subsiding and proposed that the measured ground deformation  
34  
35 140 pattern can be explained by a simple spherical source located at ~4 km beneath the caldera.  
36  
37 141 The subsidence was related to the cooling of a hydrothermal system beneath the caldera.  
38  
39 142 Lanzo *et al.* (2013) combined Cl and H<sub>2</sub>O solubility data to estimate a confining pressure of  
40  
41 143 about 50 MPa (depth ~2-3 km) for the Green Tuff magma chamber, the shallow depths being  
42  
43 144 consistent with petrological estimates for other pantellerite eruptions on the island  
44  
45 145 (Lowenstern, 1994; White *et al.*, 2005, 2009; Di Carlo *et al.*, 2010; Neave *et al.*, 2012).  
46  
47  
48  
49  
50  
51

## 52 147 **Lithostratigraphy of the Green Tuff**

53  
54  
55

1  
2  
3 148 The Green Tuff is a very complex eruptive unit, showing major lateral and vertical  
4  
5 149 heterogeneity. Primary depositional features have been obscured by various combinations of  
6  
7 150 dense welding, strong rheomorphism and revesiculation. Standard methods of correlation  
8  
9 151 along strike, such as the use of lithofacies, have proved inadequate. For example, Lanzo *et al.*  
10  
11 152 (2013) divided the tuff into five members on the basis of the clearly visible variations of some  
12  
13 153 megascopic features, including welding, crystal content and rheomorphic structures. Catalano  
14  
15 154 *et al.* (2014) grouped the many lithofacies in the tuff into three major lithostratigraphic  
16  
17 155 intervals, which show many differences in detail to the Lanzo *et al.* (2013) scheme.

18  
19  
20  
21 156 In an innovative approach, Williams *et al.* (2014) used compositional variation within the  
22  
23 157 deposit, as exemplified by Zr abundance, as a measure of stratigraphic height. They  
24  
25 158 established a type section on the Monastero scarp (Fig. 1) which shows a continuous decrease  
26  
27 159 of whole-rock Zr contents from ~2000 to 300 ppm with height within the section (Fig. 2).  
28  
29 160 Lateral correlations were then made on the basis of Zr content being a time-marker during  
30  
31 161 eruption of the tuff. It will be shown below that magma mixing was a significant process  
32  
33 162 during eruption of the tuff, such that individual whole-rock analyses may reflect the range and  
34  
35 163 proportions of mixed components. **In this report, it is assumed that the highest level in the**  
36  
37 164 **reservoir being tapped by the eruption of any given magma batch is given by the highest Zr**  
38  
39 165 **glass content in that sample.** The inferred positions of samples are consistent with the field  
40  
41 166 occurrence, where known, e.g. the basal pumice fall, **basal vitrophyre** and upper vitrophyre  
42  
43 167 (Fig. 2).  
44  
45  
46  
47  
48  
49

## 50 169 SAMPLING AND ANALYTICAL METHODS

51  
52  
53  
54  
55

1  
2  
3 170 The aims of this study included determining the range of *melt* compositions in the Green Tuff,  
4  
5 171 and studying in detail the melt–phenocryst relationships. It was critical, therefore, that,  
6  
7 172 wherever possible, pristine melt (glass) compositions were determined. The only previous  
8  
9 173 study to focus on glass compositions in the Green Tuff is that of Williams *et al.* (2014).  
10  
11 174 However, as they acknowledge, the beam diameter used in their laser ablation inductively  
12  
13 175 coupled mass spectrometry (LA-ICP-MS) determinations was sufficiently large that their  
14  
15 176 analyses probably included glass and microlites. The electron microprobe technique used here  
16  
17 177 allowed us to focus on areas of clean glass, although the presence of submicroscopic  
18  
19 178 microlites cannot be excluded in every case. Samples were collected from 15 localities  
20  
21 179 (Appendix). Glass was found in 11 samples; certain facies of the tuff, especially strongly  
22  
23 180 welded and trachytic varieties, are completely devitrified. A small number of analyses of glass  
24  
25 181 inclusions in phenocrysts have also been made.

26  
27  
28  
29 182 Two whole-rock analyses (samples 090531 and 090533) were made at Activation  
30  
31 183 Laboratories, Ancaster, Ontario, for major elements and Cu, Ni, Pb and Zn by ICP-AES  
32  
33 184 (Code 481) and other trace elements by ICP-MS (Code 4Lithoresearch), F by ion selective  
34  
35 185 electrode (Code 4F-F) and Cl by INAA (Code 4F-Cl). The remaining fifteen whole-rock  
36  
37 186 analyses were made at Bureau Veritas Commodities Canada Ltd (Table 2). Major elements  
38  
39 187 and Cr were analysed by ICP-ES, and trace elements, including REE, by ICP-MS. Mean  
40  
41 188 detection limits on major elements was close to 0.1 wt % whilst the detection limits for trace  
42  
43 189 elements varied from 0.01 to 0.1 ppm.

44  
45  
46  
47 190 Mineral compositions were determined by electron microprobe at the Inter-Institute  
48  
49 191 Analytical Complex at the Institute of Geochemistry, Mineralogy and Petrology, University of  
50  
51 192 Warsaw, using a Cameca SX-100 microprobe equipped with four wavelength dispersive  
52  
53 193 spectrometers. The analytical conditions for minerals, except feldspar, were: accelerating

1  
2  
3 194 voltage 15 kV and probe current 20-40 nA, with counting times of 20 s on peak and 10 s on  
4  
5 195 each of two background positions. For feldspar, a beam spot diameter of 5  $\mu\text{m}$  was used, to  
6  
7 196 reduce Na loss. For glass analyses, 15 kv and 6-10 nA and a dispersed spot of  $\sim 10\text{-}20 \mu\text{m}$   
8  
9 197 were used. Certain problems can arise with analysis of glass. As well as compositional  
10  
11 198 variations related to incomplete mixing of melts, melts may have been heterogeneous because  
12  
13  
14 199 of (i) proximity to different phenocrysts and (ii) contamination by microlites. In our  
15  
16 200 experience, for example, contamination by feldspar and FeTi-oxide microlites can cause some  
17  
18 201 scatter in Fe and Al abundances. We have attempted to mitigate these problems by analyzing  
19  
20 202 clear pools of matrix glass as far as possible from phenocryst phases.

23 203 The 'PAP' $\phi(\rho Z)$  program (Pouchou & Pichoir, 1991) was used for corrections. Apatite was  
24  
25 204 analysed using the technique outlined in Macdonald *et al.* (2008). Estimates of analytical  
26  
27 205 precision ( $1\sigma$ ; wt %) for all phases except glass are: Si 0.07, Ti 0.03, Al 0.02, Cr 0.02, Ni  
28  
29 206 0.03, Fe 0.09, Mn 0.03, Mg 0.04, Ca 0.08, Na 0.01, K 0.01. For glass analyses, the values are  
30  
31 207 Si 0.40, Ti 0.03, Al 0.14, Fe 0.29, Mn 0.12, Mg 0.02, Ca 0.03, Na 0.17, K 0.11, P 0.03, Zr  
32  
33 208 0.08, Cl 0.03, F 0.08. The numbers of point analyses presented are: phenocrysts: alkali  
34  
35 209 feldspar 501; fayalite 102; hedenbergite 171; FeTi-oxides 27; aenigmatite 58; apatite 10:  
36  
37 210 matrix glass and melt inclusions 145. Representative glass analyses are given in Table 3; the  
38  
39 211 full phenocryst and glass data set is given in Electronic Appendices 1-3 (available at  
40  
41 212 <http://www.petrology.oxfordjournals.org>).

## 42 43 44 45 46 47 48 214 **PETROGRAPHY**

### 49 50 51 215 **Phenocryst assemblages**

1  
2  
3 216 Phenocryst assemblages are presented in Table 1. *Alkali feldspar phenocrysts* are present in  
4  
5 217 all samples, its abundance ranging from 30-40 modal% in the comenditic trachytes to <10  
6  
7 218 modal% in the pantellerites. *Mafic phenocrysts are much less abundant, normally occurring in*  
8  
9 219 *total in amounts less than 5 modal%. Exceptions are clinopyroxene in sample 150521 (~5%)*  
10  
11 220 *and aenigmatite in 150514 (~2-3%).*

12  
13  
14 221 Whereas the alkali feldspar phenocrysts in the rhyolites tend to be euhedral to subhedral,  
15  
16 222 homogeneous and up to 3 cm across, those in the trachytes are commonly highly resorbed  
17  
18 223 (c.f. Korringa & Noble, 1972; Troll & Schmincke, 2002; *Romengo et al., 2012; D'Oriano et*  
19  
20 224 *al., 2017*) (Fig. 3 (a), (b)). Resorbed and euhedral crystals are sometimes present together in  
21  
22 225 mixed magma rocks. *Olivine* phenocrysts occur in the less peralkaline rocks, commonly  
23  
24 226 showing highly resorbed textures (Fig. 3(c)). *Clinopyroxene* is ubiquitous, varying in form  
25  
26 227 from perfectly euhedral to partially resorbed plates (Fig. 3(d)). Zoning is common, marked by  
27  
28 228 differing shades of green.

29  
30  
31  
32 229 *Quartz* phenocrysts are rounded and up to 1 cm in size. They are found only in the more  
33  
34 230 peralkaline host glasses and appear to have been of relatively late crystallization, consistent  
35  
36 231 with the observation of Di Carlo *et al.* (2010) from their experimental work on Pantescan  
37  
38 232 pantellerites. *Aenigmatite* phenocrysts, most commonly forming euhedral prisms, are also  
39  
40 233 restricted to the more peralkaline hosts. *Ilmenite* occurs throughout the whole-rock  
41  
42 234 compositional range, commonly in association with clinopyroxene and olivine but also as  
43  
44 235 discrete subhedral crystals. *Titanomagnetite* is scarcer, more texturally variable: it is present  
45  
46 236 as equant microphenocrysts, forms rims to ilmenite phenocrysts and occurs as tiny crystals  
47  
48 237 along the rims of melt inclusions. *No exsolution lamellae have been seen. Apatite*  
49  
50 238 microphenocrysts occur over the complete whole-rock compositional range, although they are  
51  
52 239 most abundant in the trachytic members. They most commonly form euhedral prismatic

1  
2  
3 240 crystals, up to a few tens of  $\mu\text{m}$  long, associated with clinopyroxene and olivine phenocrysts.  
4  
5 241 Pyrrhotite occurs in most samples, usually as small crystals ( $<20 \mu\text{m}$ ) enclosed in olivine and  
6  
7 242 clinopyroxene phenocrysts.  
8  
9

10 243 As noted above, many samples contain glass of more than one composition and the  
11  
12 244 phenocryst assemblages reflect those compositional ranges. Taking this into account, some  
13  
14 245 general observations of phenocryst distribution can be made. The two dominant assemblages  
15  
16 246 are (i) alkali feldspar + fayalite + hedenbergite + ilmenite + apatite, and (ii) alkali feldspar +  
17  
18 247 hedenbergite + aenigmatite  $\pm$  ilmenite  $\pm$  quartz + apatite. Assemblage (ii) occurs in the more  
19  
20 248 peralkaline rocks and (i) in the more trachytic types. Samples containing phases more  
21  
22 249 commonly found in melts of slightly different composition, e.g. fayalite and aenigmatite in  
23  
24 250 samples 150534 and 150551 (Table 1), contain glass of more than one composition and the  
25  
26 251 phenocryst assemblages may reflect those compositional ranges. However, it will be shown  
27  
28 252 below that the assemblage fayalite + ilmenite + aenigmatite may be in equilibrium under very  
29  
30 253 specific conditions.  
31  
32  
33  
34  
35  
36  
37  
38  
39

## 254 255 **Glass**

40 256 The majority of samples contain two or more varieties of glass, the relationships between  
41  
42 257 them being very variable. In some cases, the glasses have different colours in plane polarised  
43  
44 258 light, reflecting differing degrees of devitrification or microvesicularity without significant  
45  
46 259 compositional differences. In others, the colours reflect magma mixing, which takes several  
47  
48 260 forms. In Fig. 4(a), rounded blobs of black glass are mingled with a pale brown type. Both  
49  
50 261 types contain alkali feldspar phenocrysts. Figure 4 (b) shows streaky intermingling of dark  
51  
52 262 brown and pale glasses, feldspar phenocrysts being more common in the dark variety. Slightly  
53  
54  
55

1  
2  
3 263 denser welding in Fig. 4 (c) has resulted in mingling of narrow fiamme, the paler type being  
4  
5 264 more devitrified. The less densely welded sample in Fig. 4 (d) shows pale and slightly deeper  
6  
7 265 brown glasses patchily intermingled along their junction. No relationship between the type of  
8  
9 266 mixing and height within the deposit has been discerned.

11  
12 267 Apart from two point analyses in clinopyroxene, all analyses of melt inclusions were made  
13  
14 268 in alkali feldspar phenocrysts (Electronic Appendix 3). The inclusions are similar to those  
15  
16 269 described from the Green Tuff by Lanzo *et al.* (2013); the dominant forms are ovoidal and  
17  
18 270 subspherical, up to 250  $\mu\text{m}$  across. The analysed inclusions are composed entirely of glass.

21  
22 271

## 24 272 PHENOCRYST COMPOSITIONS

26  
27 273 *Alkali feldspar* phenocrysts are anorthoclase in the compositional range  $\text{An}_{10}\text{Ab}_{70}\text{Or}_{20}$  to  
28  
29 274  $\text{An}_0\text{Ab}_{63}\text{Or}_{37}$ , with an outlier at  $\text{Or}_{40}$  (Electronic Appendix 1(a)). The Or and Fe contents  
30  
31 275 generally increase with whole-rock peralkalinity. Barium levels ( $\leq 0.01$  apfu) are detectable  
32  
33 276 only in feldspars with  $\text{CaO} > 0.5$  wt %. The compositional range within samples is usually  
34  
35 277 small; e.g. in 150511, 150546 and 150551 the range is  $\text{Or} < 3$ . In others, e.g. 150541, a slightly  
36  
37 278 larger range ( $\text{An}_{6.2}\text{Ab}_{73.5}\text{Or}_{20.3}$  to  $\text{An}_{0.2}\text{Ab}_{68.2}\text{Or}_{31.8}$ ) reflects phenocryst occurrence in glasses  
38  
39 279 of different composition. With the exception of those with higher CaO contents ( $> 0.6$  wt %),  
40  
41 280 all the alkali feldspar phenocrysts have peralkalinity indices (P.I. = molar  
42  
43 281  $((\text{Na}_2\text{O} + \text{K}_2\text{O})/\text{Al}_2\text{O}_3)$  in the range 1.0 to 1.14.

44  
45  
46  
47 282 *Olivine* phenocryst compositions are in the range  $\text{Fo}_{6-25}$ , the Fo content decreasing with  
48  
49 283 increasing whole-rock peralkalinity (Electronic Appendix 1 (b)). They show high abundances  
50  
51 284 of MnO (3.7-4.6 wt %). Calcium levels are moderate,  $\leq 0.75$  wt % CaO, and show a positive  
52  
53 285 correlation with Fo, except for sample 150541 where the olivines are relatively Ca-poor.

286 Zoning is generally small, <1% Fo, except for one strongly resorbed crystal in 150513 where  
 287 the range is Fo<sub>9.8-6.3</sub>. The *clinopyroxene* phenocrysts are sodian hedenbergite, ranging from  
 288 Ca<sub>44</sub>Mg<sub>29</sub>Fe<sub>28</sub> to Ca<sub>37</sub>Mg<sub>9.0</sub>Fe<sub>54</sub> and with Mg-number from 51.0 to 12.5 (calculated with Fe as  
 289 Fe<sup>2+</sup>) (Electronic Appendix 1(c)). Mg-numbers decrease with increasing host-rock  
 290 peralkalinity. Oxidation ratios (Fe<sup>3+</sup>/(Fe<sup>3+</sup>+Fe<sup>2+</sup>)), calculated from stoichiometry, range from  
 291 0.01 to 0.22 and are negatively correlated with Mg-number. Sodium levels are also negatively  
 292 correlated with Mg-number, varying from 0.05 to 0.20 apfu. All are peralkaline, in the sense  
 293 of having Na/Al >1. Zonation within crystals is usually limited (≤En<sub>4</sub>) but in one crystal in  
 294 150541 En ranges from 12.8-21.7%. Clinopyroxene-melt exchange coefficients K<sup>d</sup><sup>Fe-Mg</sup>  
 295 (calculated with all Fe as Fe<sup>2+</sup>) range from 0.11-0.13. This is comparable to values (0.14-0.16)  
 296 found experimentally in a Pantescan pantellerite by Di Carlo *et al.* (2010) and in Kenyan  
 297 comendites by Scaillet & Macdonald (2003).

298 With increasing host-glass peralkalinity, the *aenigmatite* phenocrysts in the Green Tuff  
 299 contain more Na and less Ca and Al (c.f. Mahood & Stimac, 1990) (Electronic Appendix 2  
 300 (a)). The compositional variation can generally be expressed by the coupled substitution Si<sup>4+</sup>  
 301 + Na<sup>+</sup> ↔ Al<sup>3+</sup> + Ca<sup>2+</sup> (Kunzmann, 1999) (Fig. 5). The new analyses extend slightly the  
 302 compositional range on Pantelleria. *Ilmenite* phenocrysts are in the narrow range X<sub>ilm</sub> 0.95-  
 303 0.99, with Nb<sub>2</sub>O<sub>5</sub> levels ≤0.60 wt % and MnO 1.96-3.19 wt % (Electronic Appendix 2 (b)).  
 304 Limited data are available for *magnetite* (Electronic Appendix 2(b)). The phase rimming an  
 305 ilmenite phenocryst in 150513 has the composition X<sub>usp</sub> 0.47-0.49, the core of a  
 306 microphenocryst in 150541 is X<sub>usp</sub> 0.62 and an inclusion in olivine is X<sub>usp</sub> 0.72-0.76.

307 Mahood & Stimac (1990) presented analyses of *fluorapatite* in three Green Tuff rocks  
 308 spanning the compositional range trachyte to pantellerite. They noted that the REE and Si  
 309 contents and the La/Ce and La/Y ratios increased, and Ca and P contents decreased, with

1  
2  
3 310 increasing host-rock peralkalinity. Our new data (Electronic Appendix 2 (c)) largely confirm  
4  
5 311 their observations, although slightly increasing the britholite component, as measured by  
6  
7 312 REE+Y+Si contents, up to nearly 5%.  
8  
9

10 313

## 11 12 13 314 **GEOCHEMISTRY**

### 14 15 16 315 **Whole-rock compositions**

17  
18 316 **Compositional modification of peralkaline silicic rocks through secondary hydration and/or partial**  
19  
20 317 **devitrification is well established (e.g. Noble, 1967, 1970; Noble *et al.*, 1967; Baker & Henage, 1977;**  
21  
22 318 **Weaver *et al.*, 1990).** Particularly important is the potential loss of Na which affects the calculation of  
23  
24 319 the P.I. As an alternative measure of peralkalinity, White *et al.* (2003) introduced the index FK/A  
25  
26 320 (mol. (Fe+K)/Al, with all Fe calculated as Fe<sup>2+</sup>), **on the basis that Fe, K and Al are considerably less**  
27  
28 321 **mobile in aqueous systems than Na and because of the strong positive correlation between P.I. and**  
29  
30 322 **FK/Al in non-hydrated peralkaline rocks.** Plots of FK/Al against P.I. for Green Tuff rocks and glasses  
31  
32 323 show a good positive correlation (Fig. 6). However, some point analyses appear to have Na<sub>2</sub>O values  
33  
34 324 rather lower than those predicted from the FK/Al values. Loss of Na cannot, therefore, be precluded  
35  
36 325 from all our samples, especially those with high LOI values, e.g. 150542 in Table 2, **where secondary**  
37  
38 326 **hydration was the alteration process.** Evidence for the loss of Na in a vapour phase is the presence in  
39  
40 327 160541 of the rare mineral tuhualite (NaFe<sup>3+</sup>Fe<sup>2+</sup>Si<sub>6</sub>O<sub>15</sub>), which Bagiński *et al.* (2018) showed was  
41  
42 328 precipitated in vesicles during and after devitrification of the tuff. **Furthermore we cannot preclude**  
43  
44 329 **some loss of Na under the electron beam, which would be more marked in hydrated glasses.**  
45  
46

47 330 Classification of the whole-rocks has been made using the scheme for peralkaline silicic rocks of  
48  
49 331 Macdonald (1974). In the scheme, the data form a continuous trend from comenditic trachyte to  
50  
51 332 pantellerite (Fig. 7). Whole-rock compositions are plotted against SiO<sub>2</sub> in Fig. 8. With increasing  
52  
53  
54  
55

1  
2  
3 333 SiO<sub>2</sub>, Al<sub>2</sub>O<sub>3</sub>, TiO<sub>2</sub>, MgO, CaO contents decrease and Na<sub>2</sub>O and F contents increase; K<sub>2</sub>O  
4  
5 334 peaks at SiO<sub>2</sub> ~69 wt % (Fig. 8 (a)). Total Fe decreases to SiO<sub>2</sub> ~66 wt % and then increases.  
6  
7  
8 335 Barium, Sr (and Ni, Sc and V) contents are negatively correlated with SiO<sub>2</sub>, i.e. are enriched  
9  
10 336 in the trachytic members (Fig. 8 (b)). The incompatible trace elements (ITE; Be, Cs, Hf, Nb,  
11  
12 337 Rb; Ta, Th, U and Zr) generally show positive correlations with SiO<sub>2</sub> and P.I. Gallium shows  
13  
14 338 an initial increase and then the trend flattens. An important observation is that data from the  
15  
16 339 Montagna Grande Trachyte overlap with those of the Green Tuff, consistent with a genetic  
17  
18 340 relationship between them (Mahood & Hildreth, 1986).

21 341 Chondrite-normalised REE patterns for Green Tuff whole-rocks are shown in Fig. 9 (a).  
22  
23 342 The patterns are LREE-enriched; more trachytic types show gently decreasing values from Gd  
24  
25 343 to Lu, whereas the most peralkaline types have flat patterns between Gd and Lu. Europium  
26  
27 344 anomalies (Eu/Eu\*) range from 1.08 in comenditic trachyte 150522 to 0.41 in pantellerite  
28  
29 345 160541.

### 33 346 **Glass compositions**

34  
35  
36 347 Representative matrix glass compositions are given in Table 3 and the full data set in  
37  
38 348 Electronic Appendix 3. The spread in SiO<sub>2</sub> values is from 62.8 to 73.7 wt % and the glasses  
39  
40 349 range from comenditic trachyte to pantellerite (Fig. 7). Melt inclusions in phenocrysts cover a  
41  
42 350 similar compositional range (Electronic Appendix 3) and will be discussed in conjunction  
43  
44 351 with the matrix glass.

46  
47  
48 352 As noted earlier, alkali migration on devitrification and secondary hydration has affected  
49  
50 353 the melt P.I. but it appears that the glasses, including the trachytic varieties, were all  
51  
52 354 peralkaline. The compositional variations are generally similar to those in the whole-rocks,  
53  
54 355 although the range extends to both more silica-rich and less silica-rich types (Fig. 8 (a)). It

1  
2  
3 356 may also be noted that the highest Zr abundance (3183 ppm in sample 150544; Electronic  
4  
5 357 Appendix 3) is distinctly higher than the maximum recorded in previous studies of Pantescan  
6  
7 358 rocks and glass (2300 ppm; Williams *et al.*, 2014).  
8  
9

10 359 On the FeO\*-Al<sub>2</sub>O<sub>3</sub> plot (Fig. 7), the glasses show significantly more complexity than the  
11  
12 360 whole-rocks. The sub-horizontal trend across the comenditic trachyte field (Trend 1) shown  
13  
14 361 by samples 150522 and 150534 may be the result of alkali feldspar being the sole liquidus  
15  
16 362 phase in these melts, which results in an increase in FeO\*. The change in slope at ~6 wt%  
17  
18 363 FeO\* (Trend 2) could mark the onset of clinopyroxene fractionation, after which the glass  
19  
20 364 analyses follow a trend similar to the whole-rock analyses. At ~9 wt% FeO\*, two subtrends  
21  
22 365 emerge. Most glass analyses decrease sharply to ~7 wt% FeO\* at near-constant (~7-8 wt%)  
23  
24 366 Al<sub>2</sub>O<sub>3</sub> (Trend 3B). The glasses and melt inclusions at ~9 wt% FeO\* have a normative  
25  
26 367 composition very similar to the experimentally determined minimum of Carmichael &  
27  
28 368 MacKenzie (1963); we posit that this trend reflects crystallization of aenigmatite along the  
29  
30 369 quartz-feldspar cotectic, which would allow Zr, which is incompatible in all phases (Mahood  
31  
32 370 & Stimac, 1990; Neave *et al.*, 2012) to continue to increase as FeO\* decreases and P.I.  
33  
34 371 remains relatively constant ( $1.83 \pm 0.18$  for Zr >1500 ppm).  
35  
36  
37  
38

39 372 The other trend (Trend 3A) consists solely of glass and melt inclusions in sample 150514,  
40  
41 373 which continue the whole-rock trend to ~10 wt% FeO\* and 5.3 wt% Al<sub>2</sub>O<sub>3</sub> (corresponding to  
42  
43 374 P.I. = 2.61 and 2961 ppm Zr) (Table 3 and Electronic Appendix 3). These unusually low  
44  
45 375 Al<sub>2</sub>O<sub>3</sub> contents, high FeO\* contents and high P.I. make them the most evolved melts yet  
46  
47 376 recorded from Pantelleria (Fig. 7). They are, however, broadly similar to glasses (FeO\* 14-15  
48  
49 377 wt% and Al<sub>2</sub>O<sub>3</sub> 5-6 wt%) formed in the experiments of Di Carlo *et al.* (2010) and they  
50  
51 378 approach the effective minimum composition for peralkaline silicic magmas (FeO\* ~13 wt%,  
52  
53 379 Al<sub>2</sub>O<sub>3</sub> ~5 wt%) proposed by Macdonald *et al.* (2012). It is possible that pockets of highly  
54  
55

1  
2  
3 380 differentiated melt were locally developed in the Green Tuff reservoir, perhaps promoted by  
4  
5 381 unusually high F contents of the magma, as recorded in the glass in 150514 ( $\leq 0.9$  wt %  
6  
7 382 (Electronic Appendix 3). **The high F contents could have lowered melt viscosity and allowed**  
8  
9 383 **crystal fractionation to continue to slightly lower temperatures.**

10  
11  
12 384 No new REE data for glass are presented here. However, chondrite-normalized REE  
13  
14 385 patterns for data in Mahood & Stimac (1990), Neave *et al.* (2012) and Williams *et al.* (2014).  
15  
16 386 are broadly similar to those in the whole-rocks (Fig. 9 (b)). An unusual feature of several  
17  
18 387 trachytic glass and melt inclusion analyses reported in the literature is positive Eu anomalies  
19  
20 388 ( $\text{Eu}/\text{Eu}^* = 1.12\text{-}1.36$ ), accompanied by Ba concentrations up to 1308 ppm (Mahood &  
21  
22 389 Stimac, 1990; Williams *et al.*, 2014; Romano *et al.*, 2018). Positive Eu anomalies are  
23  
24 390 characteristic of Pantescan basalts that may be parental to these trachytes (Civetta *et al.*, 1998;  
25  
26 391 White *et al.*, 2009). Coupled with low plagioclase/melt partition coefficients for Eu in the  
27  
28 392 basalts (0.13; Neave *et al.*, 2012), it is possible that this is an inherited feature preserved  
29  
30 393 through fractional crystallization (Romano *et al.*, 2018). However, crystal accumulation and  
31  
32 394 resorption have also been suggested as differentiation mechanisms for the trachytes (White *et*  
33  
34 395 *al.*, 2009) and there is petrographic evidence for such a process in our samples, **such as modal**  
35  
36 396 **alkali feldspar abundances up to 40%** (Figs. 3 (a), (b)). Values higher than  $\sim 1300$  ppm Ba and  
37  
38 397  $\text{Eu}/\text{Eu}^* \approx 1.36$  have been observed only in whole-rock trachyte analyses, strongly suggesting  
39  
40 398 that those **samples** have been affected by such processes.

41  
42  
43  
44  
45 399 This raises the question as to the composition of the least evolved trachytic *melt* in the  
46  
47 400 Green Tuff. **This is important because it helps to define the liquid-line-of-descent from**  
48  
49 401 **intermediate to salic compositions.** Williams *et al.* (2014) presented LA-ICP-MS analyses of  
50  
51 402 trachytic glass with 59.90 wt %  $\text{SiO}_2$  and 251 ppm Zr. All analyses in their data set with  
52  
53  
54  
55

1  
2  
3 403 positive Eu anomalies have about the same SiO<sub>2</sub> and Zr contents. That may well represent,  
4  
5 404 therefore, the trachytic melt parental to the comenditic trachytes.  
6

7  
8 405 Chlorine values range continuously from below detection (~250 ppm) in some trachytic  
9  
10 406 glasses to 1.2 wt % (with an outlier at 1.73 wt %) in the pantellerites. Abundances are  
11  
12 407 positively correlated with SiO<sub>2</sub> and Zr, indicating progressive enrichment with increased  
13  
14 408 fractionation. Civetta *et al.* (1988), Lowenstern (1994), Gioncada & Landi (2010) and Lanzo  
15  
16 409 *et al.* (2013) noted that Cl abundances increase more quickly than Zr in glass in various  
17  
18 410 Pantescan suites, suggesting an upward enrichment mechanism in the reservoir. They also  
19  
20 411 suggested that the fact that Cl levels reached ~1 wt % and then remained constant during  
21  
22 412 further magma evolution, as measured by increases in SiO<sub>2</sub> and Zr, pointed to separation of a  
23  
24 413 Cl-bearing fluid phase with which the magmas remained in equilibrium. The new Green Tuff  
25  
26 414 data apparently show a continuing increase of Cl with fractionation, suggesting that Cl  
27  
28 415 remained in the melt phase.  
29  
30

31  
32 416 Sulphur abundances (as SO<sub>3</sub>) range from below detection (~0.03 wt %) to 0.21 wt %,  
33  
34 417 although the great majority of analyses are <0.1 wt %. These values agree with values for  
35  
36 418 Pantescan rocks given by Civetta *et al.* (1988), Lowenstern (1994), Gioncada & Landi (2010),  
37  
38 419 Neave *et al.* (2012) and Lanzo *et al.* (2013). Abundances show a positive, but scattered,  
39  
40 420 correlation with increasing peralkalinity; it is not clear whether the scatter is due to loss of S  
41  
42 421 on devitrification or to variable loss of a magmatic volatile phase.  
43  
44  
45

46 422 An important feature of the glass analyses is the range of compositions within individual  
47  
48 423 samples, shown by the SiO<sub>2</sub> and Zr ranges in Table 1, denoting the mingling in varying  
49  
50 424 combinations of trachytic and rhyolitic melts. The range within samples varies from 2 to 9 wt  
51  
52 425 % SiO<sub>2</sub> and its size is not related to the whole-rock composition. Two examples of the mixing  
53  
54 426 components are shown in Fig. 10. In Fig. 10 (a), a fragment of pale glass with a SiO<sub>2</sub> content  
55  
56 18  
57  
58  
59  
60

1  
2  
3 427 of 72-73 wt % contains irregular dark blebs with lower SiO<sub>2</sub> contents (65-68 wt %). The  
4  
5 428 photograph of a thin section of 150521(Fig. 10 (b)) shows textural intermingling of darker and  
6  
7 429 lighter glass components with SiO<sub>2</sub> values varying from ~67-71 wt %. Texturally different  
8  
9 430 glasses in the same specimen do not always show such significant compositional differences.  
10  
11 431 For example, the pale and dark glasses shown in Fig. 4 (a) have SiO<sub>2</sub> in the ranges 68.7-70.3  
12  
13 432 and 67.9-70.1 wt %, respectively.  
14  
15  
16  
17

433

## 434 GEOCHEMICAL MODELS

435 Major-element mass balance models were developed to test the fractional and equilibrium  
436 crystallization hypotheses for the origin of compositional zoning and to constrain the relative  
437 proportion of the phases involved (Table 4). All calculations were managed with Microsoft  
438 Office Excel 2013 and are considered acceptable if  $\Sigma r^2 < 1.0$ . The first model (A) tests the  
439 origin of highly evolved pantellerite glass from comenditic trachyte matrix glass. The most  
440 primitive comenditic trachyte glass analyzed for this study was recovered from sample  
441 150522, and has the lowest P.I. (1.09) and FeO\* (4.3 wt %) and highest Al<sub>2</sub>O<sub>3</sub> (16.1 wt %)   
442 observed; this was chosen as the model parent for Part A. Zirconium concentrations were  
443 below the detection limit of the electron probe for this sample. The model daughter selected  
444 is an evolved matrix glass at the intersection of two sub-trends recovered from sample 150514  
445 with P.I. = 1.96, 9.5 wt % FeO\*, 7.3 wt % Al<sub>2</sub>O<sub>3</sub> and 2591 ppm Zr.

446 A second, similar model (B) tests the origin of highly evolved pantellerite melt inclusions  
447 hosted in alkali feldspar from sample 150514 with a P.I. = 2.61, 10 wt% FeO\*, 5.3 wt%  
448 Al<sub>2</sub>O<sub>3</sub>, and 2961 ppm Zr. Both models use a mineral assemblage from sample 150511, which  
449 has a composition intermediate between the model parent and daughter. Model results are

1  
2  
3 450 both acceptable ( $\Sigma r^2 = 0.255$  and  $0.240$ , respectively) and very similar, suggesting that these  
4  
5 451 highly evolved melts can be produced by 93-94% fractional crystallization of an assemblage  
6  
7 452 dominated by alkali feldspar (92.5%) with subordinate clinopyroxene and olivine (2.5-3%  
8  
9 453 each), ilmenite (~1.5%), and apatite (<1%). This model is largely in agreement with previous  
10  
11 454 models of fractional crystallization of the peralkaline trachyte-pantellerite suite at Pantelleria,  
12  
13 455 but also presents the highest estimate for degree of fractional crystallization. The model of  
14  
15 456 White *et al.* (2009), for example, suggested 70% fractional crystallization, but from a more  
16  
17 457 peralkaline parent (P.I. = 1.12, 7.0% FeO\*) to a less peralkaline daughter (PI = 1.91, 7.8%  
18  
19 458 FeO\*). However, this and other models (e.g. Civetta *et al.*, 1998; Neave *et al.*, 2012) all agree  
20  
21 459 on a dominant role for alkali feldspar (>85% of the fractionating assemblage), with  
22  
23 460 subordinate olivine, clinopyroxene, Fe-Ti oxide, and apatite, consistent with the observed  
24  
25 461 mineral assemblages in these samples. Although we lack Zr data for the comenditic trachyte  
26  
27 462 glass, Williams *et al.* (2014) report an average value of 255 ppm for one glass sample within  
28  
29 463 the comenditic trachyte facies of the Green Tuff type section; if we assume bulk  $D_{Zr} \approx 0$ , then  
30  
31 464  $F = 0.09-0.10$  (91-90% crystallization) which is consistent with our results.  
32  
33  
34  
35

36 465 A curious feature observed in Fig. 7 is a sub-horizontal trend at ~7.5 wt %  $Al_2O_3$  (Trend  
37  
38 466 3B) that extends from the end of the main trend (modelled in Part A) to progressively lower  
39  
40 467 concentrations of FeO\* that nonetheless include glasses with the highest concentrations of Zr  
41  
42 468 measured (up to 3108 ppm) despite near-uniform Zr whole-rock concentrations (1500-1700  
43  
44 469 ppm). This trend is also manifest in Figures 11 and 12b (next section), where these samples  
45  
46 470 appear to plot along the experimental alkali feldspar-quartz cotectic (Carmichael &  
47  
48 471 MacKenzie, 1963). These highly evolved samples have assemblages characterized by a  
49  
50 472 relatively large volume of aenigmatite (e.g. 2-3% in 150514), along with quartz, alkali  
51  
52 473 feldspar and clinopyroxene; we suggest that this trend is the result of equilibrium  
53  
54  
55

1  
2  
3 474 crystallization of this assemblage. Mass balance modelling of this scheme (Table 4, Part C)  
4  
5 475 suggests its plausibility ( $\Sigma r^2 = 0.655$ , with 0.221 error from MnO), with a small degree (8%)  
6  
7 476 of late crystallization of an assemblage of aenigmatite and quartz with minor quantities of  
8  
9 477 alkali feldspar and sodian clinopyroxene resulting in a decrease in FeO\* with a slight rise in  
10  
11 478 Al<sub>2</sub>O<sub>3</sub> and P.I. An estimate of the degree of crystallization from Zr ratios (assuming  $D_{Zr} \approx 0$ ,  
12  
13 479 as above) between the model daughter and parent suggest about twice as much crystallization  
14  
15 480 (17%,  $F = 0.83$ ) as that determined by major-element mass balance modelling.  
16  
17

18  
19 481 Overall, the results of the modelling are consistent with the various magmas having been  
20  
21 482 formed by fractional crystallization of the observed phenocryst assemblages.  
22  
23

24 483

## 25 26 27 484 GEOTHERMOMETRY

28  
29 485 In Fig. 11, temperatures calculated by (a) QUILF (olivine + clinopyroxene) and (b) by  
30  
31 486 clinopyroxene – glass and clinopyroxene – whole-rock (Putirka *et al.*, 2003) (Table 5) are  
32  
33 487 plotted against Zr contents in the whole-rocks. While the QUILF results yield higher  
34  
35 488 temperatures at given Zr content, it is clear that the least evolved trachytes give ~900°C and  
36  
37 489 the temperatures then decrease to ~700°C in the most peralkaline members. There must, of  
38  
39 490 course, have been local temperature fluctuations due to mixing of magmas from different  
40  
41 491 layers. Oxygen fugacities range from FMQ-0.5 to FMQ-1.5, with an outlier at FMQ-2.2  
42  
43 492 (Table 5). The temperature and  $fO_2$  estimates are similar to those for Pantescan pantellerites  
44  
45 493 calculated thermodynamically by White *et al.* (2005, 2009) and determined experimentally by  
46  
47 494 Di Carlo *et al.* (2010). Thermodynamic values recovered by olivine – clinopyroxene  
48  
49 495 equilibria in the QUILF system are pressure-sensitive, but for an increase (or decrease) of 500  
50  
51 496 bars of pressure, silica activity changes by only 0.02 units and temperature increases (or  
52  
53  
54  
55

1  
2  
3 497 decreases) by only 3°C on average. However, oxygen fugacity, relative to the FMQ buffer,  
4  
5 498 remains relatively unchanged.  
6

7  
8 499 Whole-rock (a) and glass (b) analyses have been plotted in the system Q-Ab-Or-H<sub>2</sub>O with 8.3 mol%  
9  
10 500 aegirine + 8.3 mol% sodium metasilicate added, P<sub>H<sub>2</sub>O</sub> = 1000 bar, and projected from H<sub>2</sub>O + aegirine +  
11  
12 501 sodium metasilicate (Carmichael & MacKenzie, 1963) (Fig. 12). The normative mineralogy was  
13  
14 502 calculated with FeO/FeO\* = 0.9, corresponding to oxygen fugacities buffered at FMQ-1 between 700  
15  
16 503 and 900°C (Sack *et al.*, 1980). The alkali feldspar liquidus surface is plotted as crosses, labelled with  
17  
18 504 the experimentally determined temperature (°C) for that composition. The minimum for this system  
19  
20 505 occurs at Q<sub>40.5</sub>Or<sub>34.5</sub>Ab<sub>25</sub>, with the alkali feldspar-quartz cotectic located at approximately Q<sub>40</sub>. Also  
21  
22 506 shown is the “thermal valley” of Carmichael & MacKenzie (1963), the differentiation path of a system  
23  
24 507 undergoing crystal fractionation of alkali feldspar with a composition of ~Or<sub>35</sub>. Despite some scatter,  
25  
26 508 temperatures drop from 825°C in the trachytes to 700°C in the most peralkaline whole-rocks,  
27  
28 509 temperatures consistent with those found in Fig. 11, and the rocks generally follow a feldspar  
29  
30 510 fractionation trend. The spread of glass compositions at Or<sub>40</sub> is consistent with some melts having  
31  
32 511 reached the quartz-feldspar cotectic.  
33

34 512 The vertical decrease in temperature from the comenditic trachyte to the pantellerite is accompanied  
35  
36 513 by an increase in silica activity relative to quartz saturation ( $a_{\text{SiO}_2}$  (Qtz)), **calculated by QUILF95**,  
37  
38 514 from 0.74 to 1.0, as well as a slight increase in oxygen fugacity relative to the FMQ buffer (Fig. 13).  
39  
40 515 Macdonald *et al.* (2011) described the antipathetic relationship between fayalitic olivine and  
41  
42 516 aenigmatite as a function of T, P and  $a_{\text{SiO}_2}$ , with the latter crystallizing at the expense of the former at  
43  
44 517 T < 750°C at silica activities close to or at quartz saturation at 150 MPa. Lower pressures extend the  
45  
46 518 stability of aenigmatite to higher temperatures (cf. White *et al.*, 2005; Di Carlo *et al.*, 2010) which is  
47  
48 519 consistent with these results.  
49

50  
51 520 **Fayalite-bearing rhyolites with ilmenite present as the sole Fe-Ti oxide phase crystallize in T-fO<sub>2</sub>**  
52  
53 521 **space along the displaced FHQ (fayalite-hematite-quartz) buffer. In this sense, the FHQ buffer is**  
54  
55 522 **“displaced” from that which would plot for unit activities for all phases. A regression through the T-**  
56  
57 22

1  
2  
3 523  $a_{\text{SiO}_2}$  data was used to calculate the displaced FHQ buffer for ilmenite compositions between  $X_{\text{ilm}}$   
4 524 0.95 and 0.98 in Fig. 13. In our formulation, unit activity is assumed only for fayalite and the curve is  
5 525 displaced to lower  $f_{\text{O}_2}$  due to much lower hematite activities ( $X_{\text{hem}} = 0.03\text{-}0.05$ ; activities calculated  
6 526 following Andersen & Lindsley, 1988) and silica activities relative to quartz saturation less than one  
7 527 (interpolated from the linear trend in the previous figure, with silica activities calculated from olivine-  
8 528 clinopyroxene equilibrium using QUILF95).

9  
10  
11  
12  
13  
14  
15 529 The Green Tuff broadly follows the FHQ curve, with the magma chamber becoming slightly less  
16 530 reduced roofward relative to the FMQ buffer. A comparison with experimental data from pantelleritic  
17 531 systems, including Eburru, Kenya (Scaillet & Macdonald, 2006) and Pantelleria (Di Carlo *et al.*,  
18 532 2010), suggests that this may be due to a corresponding volatile gradient from ~1 wt % H<sub>2</sub>O in the  
19 533 comenditic trachyte to ~4 wt % H<sub>2</sub>O in the pantellerite. The presence of such a volatile gradient may  
20 534 be supported by FTIR analyses of melt inclusions in the basal pantellerite and uppermost trachyte.  
21 535 Melt inclusions in the trachyte are comenditic trachyte in composition, with 0.15-1.05 wt % H<sub>2</sub>O  
22 536 (Romano *et al.*, submitted). Lanzo *et al.* (2013) reported values of up to 4.2 wt % H<sub>2</sub>O from feldspar-  
23 537 hosted melt inclusions in the pantelleritic basal fall unit, consistent with values from melt inclusions in  
24 538 compositionally similar pantellerite lavas (up to 4.9 wt % H<sub>2</sub>O; Gioncada & Landi, 2010; Neave *et al.*,  
25 539 2012).

26  
27  
28  
29  
30  
31  
32  
33  
34  
35  
36  
37  
38 540 Using the model parameters of White *et al.* (2009), the simplest explanation for a volatile  
39 541 gradient is ~70% fractional crystallization of a comenditic trachyte melt with 1.0-1.5 wt %  
40 542 H<sub>2</sub>O, which would produce a pantellerite melt with 3.3-4.9 wt % H<sub>2</sub>O (assuming bulk  $D_{\text{H}_2\text{O}} =$   
41 543 0.01). This in turn would require 0.3-0.5 wt % H<sub>2</sub>O in the parental basalts – lower than either  
42 544 the 0.9-1.6 wt % reported by Gioncada & Landi (2010) for melt inclusions in the Cuddie  
43 545 Rosse basalt or the 1.0-1.5 wt % predicted from MELTS modelling (White *et al.*, 2009).  
44 546 Experimental results on Pantescan basalts also suggest that they must be hydrous ultimately to  
45 547 produce pantelleritic melts (Scaillet *et al.*, 2005), although the MELTS results reported by  
46 548 White *et al.* (2009) suggest that basalt water concentrations as low as 0.5 wt % would also  
47  
48  
49  
50  
51  
52  
53  
54  
55  
56  
57  
58  
59  
60

1  
2  
3 549 produce similar comenditic trachyte. The volatile gradient and accompanying change in  
4  
5 550 oxidation state could also be explained by melt vesiculating, which could result in a reaction  
6  
7 551 between Fe-rich silicate melt and H<sub>2</sub>O *via* thermal dissociation and degassing of H<sub>2</sub> (cf.  
8  
9 552 Carmichael, 1991; Mungall & Martin, 1995; Scaillet & Macdonald, 2001; White *et al.*, 2005).

10  
11  
12 553

## 15 554 **DISCUSSION**

16  
17 555

### 19 556 **Nature of Green Tuff reservoir**

21 557 Possible relationships in the plumbing system prior to the eruption of the Green Tuff are  
22  
23 558 shown in Fig. 17. A magma reservoir is envisaged with a trachytic crystal mush overlain by a  
24  
25 559 layered pantelleritic upper part of the chamber. **Pressure estimates of 100 MPa, which**  
26  
27 560 **correspond to depths of 3-4 km, were used for all thermodynamic calculations because (1) this**  
28  
29 561 **is in between the total range of 50-150 MPa estimated by previous workers for the depth of**  
30  
31 562 **the magma chamber using various methods, and (2) this depth is consistent with geophysical**  
32  
33 563 **studies of the depth of the magma chamber, e.g. with the model of Mattia *et al.* (2007), based**  
34  
35 564 **on geodetic data, placing the top of the reservoir at ~4 km beneath the caldera. The overall**  
36  
37 565 **depth of the reservoir would have been greater if the Montagna Grande trachytes were part of**  
38  
39 566 **the magma system; they were erupted from lower layers in the reservoir during resurgence**  
40  
41 567 **following eruption of the Green Tuff, although the depth of magma being tapped is not**  
42  
43 568 **known. Major element contents are consistent with such a **cogenetic** relationship (Fig. 8 (a))**  
44  
45 569 **and, although trace element data are rather scarce for Montagna Grande, the trace elements**  
46  
47 570 **are also consistent; average Zr/Nb ratios, for example, are 4.9 in the Green Tuff and 4.5 in the**  
48  
49 571 **Montagna Grande trachytes. The speculative gabbroic mush represents the source of the**  
50  
51 572 **trachytic magmas, squeezed out either by compaction or buoyancy.**

1  
2  
3 573 Similar models for trachyte – peralkaline rhyolite relationships have been proposed by  
4  
5 574 Troll & Schmincke (2001) for ignimbrite ‘A’, Gran Canaria, and by Sumner & Wolff (2003)  
6  
7 575 for the ‘TL’ ignimbrite, Gran Canaria.  
8  
9

10 576

### 11 577 **Origin of compositional zonation**

12  
13  
14 578 Previous authors have used geochemical modelling to show that the transition from trachyte  
15  
16 579 to rhyolite at Pantelleria can be satisfactorily modelled by fractionation of an alkali feldspar-  
17  
18 580 olivine-clinopyroxene-oxide  $\pm$  aenigmatite assemblage (Civetta *et al.*, 1988; White *et al.*,  
19  
20 581 2009; Neave *et al.*, 2012). The new models presented here are consistent with these earlier  
21  
22 582 models. Experimental studies of Pantescan rocks by Di Carlo *et al.* (2010) and Romano *et al.*  
23  
24 583 (2018) are also consistent with such models. We propose, therefore, that the comenditic  
25  
26 584 trachytes separated from the crystal-rich metaluminous trachytes later erupted as the  
27  
28 585 Montagna Grande Trachyte. Continued fractional crystallization of the trachytic magmas  
29  
30 586 generated pantelleritic melts which separated from the trachytes through buoyancy effects and  
31  
32 587 accumulated towards the roof of the reservoir, finding levels determined by their density.  
33  
34  
35

36 588 Some of the compositional variation in the Green Tuff has also been related to alkali  
37  
38 589 feldspar accumulation (Korringa & Noble, 1972; Prosperini *et al.*, 1990; White *et al.*, 2009).  
39  
40 590 For example, the so-called low-incompatible trace element (low-ITE) trachytes of White *et al.*  
41  
42 591 (2009) were shown to contain up to 47% modally of alkali feldspar phenocrysts. The new data  
43  
44 592 set provides further evidence that the process was important in the evolution of the Green  
45  
46 593 Tuff. For example, at ~300 ppm Zr, the Eu anomaly increases from 1 to 1.6 (Fig. 14). At the  
47  
48 594 same Zr value, K/Rb ratios rise from ~600 to 1000, Ba contents from ~700-2300 ppm and Sr  
49  
50 595 contents from ~50 to 70 ppm, features consistent with feldspar accumulation in the trachytic  
51  
52 596 rocks. Major- and trace- element models presented by White *et al.* (2009) and Romano *et al.*  
53  
54  
55

56 25  
57  
58  
59  
60

1  
2  
3 597 (2018) suggest that samples affected by accumulation or resorption of alkali feldspar will  
4  
5 598 have Ba >1300 ppm. The process was also locally operative at higher levels in the chamber;  
6  
7 599 sample 150541, with ~35 modal% feldspar phenocrysts, has high Al<sub>2</sub>O<sub>3</sub>, Ba and Sr (Fig. 8)  
8  
9 600 contents. However, it has a negative Eu anomaly (Eu/Eu\* 0.54) which would require that the  
10  
11 601 accumulating feldspar had a negative anomaly. Yet Mahood & Stimac (1990) argued that all  
12  
13 602 the feldspars in the Green Tuff have strong positive Eu anomalies.  
14  
15

16 603 It appears, therefore, that the composition of the comenditic trachyte underlying the  
17  
18 604 pantellerites was modified by variable amounts of feldspar accumulation.  
19  
20

21 605

### 22 606 **Glass heterogeneity and implications for syneruptive mixing**

23  
24  
25  
26 607 Density variations in the melts (glasses) have been calculated by the method of Bottinga &  
27  
28 608 Weill (1970) (Fig. 15). Anhydrous densities range from 2480 kg m<sup>-3</sup> in the trachytes to 2420  
29  
30 609 kg m<sup>-3</sup> in the most peralkaline melts. This might imply that the pantelleritic part of the  
31  
32 610 reservoir was stably density-stratified while the higher density and viscosity of the feldspar-  
33  
34 611 rich trachytes prevented them from rising and mixing with the overlying rhyolites. This  
35  
36 612 further implies that eruption of the Green Tuff was triggered by an external mechanism. We  
37  
38 613 suggest that the trigger was an influx of more mafic magma into the trachytic parts of the  
39  
40 614 reservoir which raised temperatures (as seen in the resorption of phenocrysts) and caused  
41  
42 615 trachytic melts to rise and mix with the overlying more evolved melts (c.f. Flude *et al.*, 2008;  
43  
44 616 Romengo *et al.*, 2012). Triggering of the eruption of peralkaline magmas by intrusion of  
45  
46 617 intermediate magmas has been proposed by Sumner & Wolff (2003) for ignimbrite 'TL'  
47  
48 618 (Gran Canaria) and by Pimentel *et al.* (2016) for comenditic trachytes of the AD 1761  
49  
50 619 eruption at Terceira Island (Azores). The lack of significant compositional zoning in the  
51  
52 620 resorbed phenocrysts is taken to show that the more mafic magma acted as a heat source  
53  
54  
55

56 26  
57  
58  
59  
60

1  
2  
3 621 without physical or chemical mixing, as discussed by D'Oriano *et al.* (2017) for similar  
4  
5 622 feldspar-rich zones for comenditic trachytes of the Lajes ignimbrite eruption, Terceira Island,  
6  
7 623 Azores.

8  
9  
10 624 Models of magma evacuation from compositionally zoned chambers have shown how each  
11  
12 625 successive evacuation draws magma from progressively deeper levels of the chamber,  
13  
14 626 isochemical surfaces being deflected upwards beneath the vents so that several compositional  
15  
16 627 layers can be tapped simultaneously (Blake, 1981; Blake & Ivey, 1986; Spera *et al.*, 1986;  
17  
18 628 Schuraytz *et al.*, 1989; Macdonald *et al.*, 1994). It was noted earlier that many Green Tuff  
19  
20 629 samples show a range of matrix glass compositions, denoting the mingling in varying  
21  
22 630 combinations of trachytic and rhyolitic melts. Importantly, the mingling was very thorough,  
23  
24 631 down to the micron scale, which we ascribe to the small differences in temperature and  
25  
26 632 density between the pantelleritic melts which did not significantly hinder mixing.

27  
28  
29  
30 633 The range of SiO<sub>2</sub> values in the glasses is matched by variations in Zr (Table 1). It appears,  
31  
32 634 therefore, that the steady increase in Zr values shown with increasing height in the pre-  
33  
34 635 eruptive chamber by Williams *et al.* (2014) does not simply reflect an increasing degree of  
35  
36 636 fractionation of the melt upwards. Rather, it reflects an increasing proportion of evolved melts  
37  
38 637 in earlier erupted magma batches. Plotting the highest Zr value in each sample, as a measure  
39  
40 638 of the sample's highest stratigraphic position within the pre-eruptive chamber, against the  
41  
42 639 range of Zr contents in the same glasses, two broad zones can be distinguished (Fig. 16): (i) a  
43  
44 640 zone where the glasses all have rather homogeneous (?) trachytic composition; and (ii) a zone  
45  
46 641 where the glasses are dominantly mixes of rhyolitic-rhyolitic melts. Two barriers to mixing  
47  
48 642 thus existed in the system: one between crystal-rich and crystal-poor comenditic trachytes and  
49  
50 643 one between the trachytes and pantellerites.

1  
2  
3 644 An important general point arising from the within-sample ranges in glass composition is  
4  
5 645 that whole-rock analyses do not necessarily give a true indication of the range of melt  
6  
7 646 compositions in the pre-eruptive reservoir; as noted above, the highest whole-rock and glass  
8  
9 647 Zr values are 2300 and 3183 ppm, respectively. This raises the question as to how common  
10  
11 648 this type of fine-scale mingling may be in compositionally zoned silicic systems. Clearly,  
12  
13 649 relevant studies would preferably need to be made in systems preserving significant glassy  
14  
15 650 facies. However, in their absence a careful analysis of the stability relationships of the  
16  
17 651 phenocryst assemblages should provide clues as to the range of host melts.  
18  
19  
20  
21 652

### 22 23 24 653 **Significance for the Daly Gap**

25  
26 654 Models for the formation of the Pantescan suite are broadly divisible into two groups. In one,  
27  
28 655 the trachytes and rhyolites were formed independently of basaltic magma; intermediate  
29  
30 656 compositions (mugearites and benmoreites) are the products of magma mixing (Lowenstern &  
31  
32 657 Mahood, 1991; Avanzinelli *et al.*, 2004; Ferla & Meli, 2006; Romengo *et al.*, 2012). In the  
33  
34 658 other model, the salic rocks were formed by the prolonged crystal fractionation of basaltic  
35  
36 659 magma. The observed scarcity or absence of intermediate rocks results from either a physical  
37  
38 660 or thermodynamic discrimination in the magma reservoirs and their non-eruption (Civetta *et*  
39  
40 661 *al.*, 1988; White *et al.*, 2009; Neave *et al.*, 2012). One aim of this paper has been to assess  
41  
42 662 whether melts of intermediate composition were present in the Green Tuff magma system.  
43  
44 663 Some of the published evidence is equivocal. Geochemical modelling had shown that the  
45  
46 664 pantellerites of Pantelleria could have been produced by ~95% fractional crystallization of  
47  
48 665 parental alkali basalts, *via* magmas of intermediate composition. In the modelling of White *et*  
49  
50 666 *al.* (2009), melts entered the Daly gap (~50-62 wt % SiO<sub>2</sub>) after 30% crystallization, and then  
51  
52 667 stayed there for a further 59% crystallization. In contrast, in experiments made on a Pantescan  
53  
54  
55  
56  
57  
58  
59  
60 28

1  
2  
3 668 basalt at 1 atm and 8 kb, Mahood & Baker (1986) found that residual melts had not reached  
4  
5 669 the Daly gap after 70% crystallization.  
6

7  
8 670 The main approach used here was to carefully relate glass and mineral compositions to  
9  
10 671 textures. The least evolved glass composition in the new Green Tuff data set has 62.84 wt %  
11  
12 672 SiO<sub>2</sub>; similar glass compositions (SiO<sub>2</sub> 59.90-62.3 wt %) have been recorded in the Green  
13  
14 673 Tuff by Mahood & Stimac (1990) and Williams *et al.* (2014). No clearly intermediate-  
15  
16 674 composition melts have thus been found.  
17

18  
19 675 As an indicator of what mineral compositions might be expected, in their MELTS  
20  
21 676 modelling of the evolution of Pantescan suites White *et al.* (2009) found the following  
22  
23 677 mineral compositions as melts passed through the benmoreite stage (at 1.0% H<sub>2</sub>O in the  
24  
25 678 parent, 100 MPa, FMQ-1): plagioclase An<sub>60-49</sub>; olivine Fo<sub>47-21</sub>; clinopyroxene Wo<sub>45</sub>En<sub>35-30</sub>Fs<sub>20-</sub>  
26  
27 679 <sub>25</sub>. For this study, a careful analysis was made of the cores of phenocrysts in the Green Tuff,  
28  
29 680 on the basis that they may have preserved compositions from earlier stages of magma  
30  
31 681 evolution. For feldspar, the most “mafic” composition was An<sub>7,9</sub>; for olivine Fo<sub>25,4</sub>; for  
32  
33 682 clinopyroxene En<sub>29</sub>. The main phenocryst phases thus crystallized from melts more evolved  
34  
35 683 than benmoreite.  
36  
37

38  
39 684 White *et al.* (2009) described, from post-caldera trachyte lavas of Montagna Grande and  
40  
41 685 Monte Gibe, anorthoclase phenocrysts (An<sub>3-9</sub>Ab<sub>70-71</sub>Or<sub>20-26</sub>) with cores of resorbed  
42  
43 686 plagioclase (An<sub>34</sub>Ab<sub>62</sub>Or<sub>4</sub>). A benmoreitic lava from Montagna Grande, thought to have  
44  
45 687 formed by mixing of trachytic and mafic magmas, contains feldspar phenocrysts with  
46  
47 688 resorbed cores of plagioclase (An<sub>43-32</sub>Ab<sub>53-63</sub>Or<sub>3-5</sub>) mantled by oligoclase (An<sub>23-25</sub>Ab<sub>66-67</sub>Or<sub>9-</sub>  
48  
49 689 <sub>11</sub>) (Romengo *et al.*, 2012). The occurrence of such calcic compositions *as cores* suggests that  
50  
51 690 the feldspars initially crystallized from magmas of intermediate composition and were being  
52  
53 691 resorbed during subsequent melt evolution. It is possible that if the Montana Grande trachytes  
54  
55  
56  
57  
58  
59  
60

1  
2  
3 692 were part of the Green Tuff magma system (Mahood & Hildreth, 1986), benmoreitic magmas  
4  
5 693 may have been trapped in these lower, dense and viscous levels in the chamber and could not  
6  
7 694 rise into the part erupted as the Green Tuff. Many post-Green Tuff pantelleritic eruptives have  
8  
9 695 abundant trachytic enclaves (Prosperini *et al.*, 1990; Ferla & Meli, 2006; Landi & Rotolo,  
10  
11 696 2015), implying ready intrusion of trachyte to high-levels in these systems. This suggests a  
12  
13 697 remarkable efficiency for the trachyte “trap” zone in the Green Tuff reservoir. It may be noted  
14  
15 698 that Mattia *et al.* (2007) suggested that trapping of benmoreitic and mugearitic magmas in the  
16  
17 699 chamber due to their relatively high density compared to the more peralkaline rocks and  
18  
19 700 contributed to the high values of the Bouguer anomaly.  
20  
21  
22

23 701 In summary, possible relationships in the plumbing system prior to the eruption of the  
24  
25 702 Green Tuff are shown in Fig. 17. The upper part of the erupted reservoir is compositionally  
26  
27 703 zoned pantellerite magma, underlain by feldspar-phyric trachyte. The crystal-rich colourless  
28  
29 704 layer would be erupted during resurgence as the Montagna Grande lavas. The gabbroic mush  
30  
31 705 represents the source of the trachytic magmas, squeezed out either by compaction or  
32  
33 706 buoyancy.  
34  
35  
36  
37  
38  
39

## 40 708 **CONCLUSIONS**

41  
42 709 (1) The Green Tuff was erupted from a magma reservoir compositionally zoned from  
43  
44 710 pantellerite (top) to comenditic trachyte (bottom). Conditions within the reservoir are  
45  
46 711 estimated to have been temperature ~900-700 °C,  $f_{O_2}$  FMQ-1.5 to FMQ-0.5 and  $a_{SiO_2}$  (relative to  
47  
48 712 quartz saturation) 0.74-1.00.  
49  
50  
51  
52  
53  
54  
55

1  
2  
3 713 (2) The trachytic layer was rich in alkali feldspar phenocrysts and overlay the densely-phyric  
4  
5 714 Montagna Grande Trachyte, which was erupted during resurgence of the caldera whose  
6  
7 715 formation accompanied eruption of the Green Tuff.  
8  
9

10 716 (3) Prior to eruption, the Green Tuff magma was layered by crystal fractionation of alkali  
11  
12 717 feldspar- olivine-clinopyroxene-Fe-Ti oxide- apatite assemblages.  
13  
14

15 718 (4) During eruption, mingling between layers, especially in the pantellerites, was ubiquitous,  
16  
17 719 at scales down to the micron level, a process revealed only by detailed analysis of within-  
18  
19 720 sample glasses. Whole-rock analyses mask the significance of the mixing.  
20  
21

22 721 (5) The new glass analyses have significantly extended the range of melt compositions in the  
23  
24 722 tuff, to those approaching the effective minimum composition for peralkaline silicic melts of  
25  
26 723 Macdonald *et al.* (2012).  
27  
28

29 724 (6) Phenocrysts in the comenditic trachyte are commonly heavily resorbed but only slightly  
30  
31 725 zoned compositionally, indicating perhaps that they were heated by, but did not mix, with  
32  
33 726 influxes of intermediate magmas which were trapped in a lower layer.  
34  
35

36  
37 727

## 38 39 40 728 **ACKNOWLEDGEMENTS**

41  
42  
43 729 We thank Lidia Jezak for help with the electron microprobe analyses. Wes LeMasurier, David  
44  
45 730 Neave, Silvio Rotolo and Editor Gerhard Wörner provided extremely detailed and helpful  
46  
47 731 reviews of the manuscript.  
48  
49

50 732

## 51 52 733 **REFERENCES**

53  
54 734 Andersen, D.J. & Lindsley, D.H. (1988) Internally consistent solution models for Fe-Mg-Mn-Ti  
55

- 1  
2  
3 735 oxides. *American Mineralogist* **73**, 714-726.
- 4  
5 736 Andersen, D.J., Lindsley, D.H. & Davidson, P.M. (1993). QUILF: a PASCAL program to assess  
6  
7 737 equilibria among Fe-Mg-Mn-Ti oxides, pyroxenes, olivine, and quartz. *Computers and Geosciences*  
8  
9 738 **19**, 1333-1350.
- 10  
11 739 Avanzinelli, R., Bindi, L., Menchetti, S. & Conticello, S. (2004). Crystallization and genesis of  
12  
13 740 peralkaline magmas from Pantelleria Volcano, Italy: an integrated petrological and crystal-chemical  
14  
15 741 study. *Lithos* **73**, 41-69.
- 16  
17  
18 742 Bagiński, B., Macdonald, R., White, J.C. & Ježak, L. (2018). Tuhualite in a peralkaline rhyolitic  
19  
20 743 ignimbrite from Pantelleria, Italy. *European Journal of Mineralogy*. DOI: 10.1127/ejm/2018/0030-  
21  
22 744 2711.
- 23  
24  
25  
26  
27 745 Baker, B.H. & Henage, I.F. (1977). Compositional changes during crystallization of some peralkaline  
28  
29 746 silicic lavas of the Kenya Rift Valley. *Journal of Volcanology and Geothermal Research* **2**, 17-28.
- 30  
31  
32 747 Behncke, B., Berrino, G., Corrado, G. & Velardita, R. (2006). Ground deformation and gravity  
33  
34 748 changes on the island of Pantelleria in the geodynamic framework of the Sicily Channel. *Journal of*  
35  
36 749 *Volcanology and Geothermal Research* **150**, 146-162.
- 37  
38  
39  
40  
41 750 Blake, S. (1981). Eruptions from zoned magma chambers. *Journal of the Geological Society, London*  
42  
43 751 **138**, 281-287.
- 44  
45  
46 752 Blake, S. & Ivey, G.N. (1986). Magma mixing and the dynamics of withdrawal from stratified  
47  
48 753 reservoirs. *Journal of Volcanology and Geothermal Research* **27**, 153-178.
- 49  
50  
51  
52 754 Bottinga, Y. & Weill, D.F. (1970). Densities of liquid silicate systems calculated from partial molar  
53  
54 755 volumes of oxide components. *American Journal of Science* **269**, 169-182.

- 1  
2  
3 756 Calò, M. & Parisi, L. (2014). Evidences of a lithospheric fault zone in the Sicily Channel  
4  
5 757 continental rift (southern Italy) from instrumental seismicity data. *Geophysical Journal*  
6  
7 758 *International* **199**, 219-225.
- 8  
9 759 Carmichael, I.S.E. (1991). The redox states of basic and silicic magmas: a reflection of their source  
10  
11 760 regions? *Contributions to Mineralogy and Petrology* **106**, 129-141.
- 12  
13  
14 761 Carmichael, I.S.E. & Mackenzie, W.S. (1963). Feldspar-liquid equilibria in pantellerites: an  
15  
16 762 experimental study. *American Journal of Science* **261**, 382-396.
- 17  
18  
19  
20 763 Catalano, S., Tortorici, L. & Viccaro, M. (2014). Regional tectonic control on large size explosive  
21  
22 764 eruptions: Insights into the Green Tuff ignimbrite unit of Pantelleria. *Journal of Geodynamics* **73**,  
23  
24 765 223-233.
- 25  
26  
27  
28 766 Chapman, D.S. & Pollack, H.N. (1975). Global heat flow: A new look. *Earth and Planetary Science*  
29  
30 767 *Letters* **28**, 23-32.
- 31  
32  
33  
34 768 Civetta, L., Cornette, Y., Crisci, G., Gillot, P.Y., Orsi, G. & Requejo, C.S. (1984). Geology,  
35  
36 769 geochronology and chemical evolution of the island of Pantelleria. *Geological Magazine* **121**, 541-  
37  
38 770 562.
- 39  
40  
41  
42 771 Civetta, L., Cornette, Y., Gillot, P.Y. & Orsi, G. (1988). The eruptive history of Pantelleria (Sicily  
43  
44 772 Channel) in the last 50 ka. *Bulletin of Volcanology* **50**, 47-57.
- 45  
46  
47  
48 773 Civetta, L., D'Antonio, M., Orsi, G. & Tilton, G.R. (1998). The geochemistry of volcanic rocks from  
49  
50 774 Pantelleria island, Sicily channel: Petrogenesis and characteristics of the mantle source region.  
51  
52 775 *Journal of Petrology* **39**, 1453-1491.

- 1  
2  
3 776 Civile, D., Lodolo, E., Tortorici, L., Lanzafame, G. & Brancolini, G. (2008). Relationships between  
4  
5 777 magmatism and tectonics in a continental rift: the Pantelleria Island region (Sicily Channel, Italy).  
6  
7  
8 778 *Marine Geology* **251**, 32-46.  
9  
10  
11 779 Della Vedova, B., Lucazeau, F., Pasquale, V., Pellis, G. & Verdoya, M. (1995). Heat flow in the  
12  
13 780 tectonic provinces crossed by the southern segment of the European Geotraverse. *Tectonophysics*  
14  
15 781 **244**, 57-74.  
16  
17  
18  
19 782 Di Carlo, I., Rotolo, S., Scaillet, B., Buccheri, V. & Pichavant, M. (2010). Phase equilibrium  
20  
21 783 constraints on pre-eruptive conditions of recent explosive volcanism of Pantelleria Island, Italy.  
22  
23 784 *Journal of Petrology* **51**, 2245-2276.  
24  
25  
26  
27 785 D'Oriano, C., Landi, P., Pimentel, A. & Zanon, V. (2017). Magmatic processes revealed by  
28  
29 786 anorthoclase textures and trace element modelling: The case of the Lajes Ignimbrite eruption  
30  
31 787 (Terceira Island, Azores). *Journal of Volcanology and Geothermal Research* **347**, 44-63.  
32  
33  
34  
35  
36 788 Esperança, S. & Crisci, G.M. (1995). The island of Pantelleria: A case for the development of DMM-  
37  
38 789 HIMU isotopic compositions in a long-lived extensional setting. *Earth and Planetary Science*  
39  
40 790 *Letters* **136**, 167-182.  
41  
42  
43  
44 791 Ferla, P. & Meli, C. (2006). Evidence of magma mixing in the 'Daly Gap' of alkaline suites: a case  
45  
46 792 study from the enclaves of Pantelleria (Italy). *Journal of Petrology* **47**, 1467-1502.  
47  
48  
49  
50 793 Flude, S., Burgess, R. & McGarvie, D.W. (2008). Silicic volcanism at Ljósufjöll, Iceland: Insights into  
51  
52 794 evolution and eruptive history from Ar-Ar dating. *Journal of Volcanology and Geothermal*  
53  
54 795 *Research* **169**, 154-175.  
55

- 1  
2  
3 796 Frost, B.R., Lindsley, D.H. & Andersen, D.J. (1988). Fe-Ti oxide-silicate equilibria: assemblages with  
4  
5 797 fayalitic olivine. *American Mineralogist* **73**, 727-740.  
6  
7  
8 798 Fulignati, P., Malfitano, G. & Sbrana, A. (1997). The Pantelleria caldera geothermal system: Data  
9  
10  
11 799 from the hydrothermal minerals. *Journal of Volcanology and Geothermal Research* **75**, 251-270.  
12  
13  
14 800 Gantar, C., Morelli, C., Segre, A. & Zampieri, L. (1961). Studio gravimetrico e considerazioni  
15  
16 801 geologiche sull'isola di Pantelleria. *Bollettino Geofisica Teorica e Applicata* **3**, 267-287.  
17  
18  
19 802 Gioncada, A. & Landi, P. (2010). The pre-eruptive volatile contents of recent basaltic and pantelleritic  
20  
21 803 magmas at Pantelleria (Italy). *Journal of Volcanology and Geothermal Research* **189**, 191-201.  
22  
23  
24 804 Jordan, N.J., Rotolo, S.G., Williams, R., Speranza, F., McIntosh, W.C., Branney, M.J. & Scaillet, S.  
25  
26 805 (2018). Explosive eruptive history of Pantelleria, Italy: Repeated caldera collapse and ignimbrite  
27  
28 806 emplacement at a peralkaline volcano. *Journal of Volcanology and Geothermal Research* **349**, 47-  
29  
30  
31 807 73.  
32  
33  
34  
35 808 Korringa, M.K. & Noble, D.C. (1972). Genetic significance of chemical, isotopic, and petrographic  
36  
37 809 features of some peralkaline salic rocks from the island of Pantelleria. *Earth and Planetary Science*  
38  
39 810 *Letters* **17**, 258-262.  
40  
41  
42  
43 811 Kovalenko, V.I., Naumov, V.B., Solovova, I.P., Giris, A.V., Hervig, R.L. & Boriani, A. (1994).  
44  
45 812 Volatile components, composition, and crystallization conditions of the Pantelleria basalt-  
46  
47 813 pantellerite association magmas, inferred from the melt and fluid inclusion data. *Petrology* **2**, 19-34.  
48  
49  
50 814 Kunzmann, T. (1999). The aenigmatite-rhönite mineral group. *European Journal of Mineralogy* **11**,  
51  
52 815 743-756.  
53  
54  
55  
56 35  
57  
58  
59  
60

- 1  
2  
3 816 Landi, P. & Rotolo, S.G. (2015). Cooling and crystallization recorded in trachytic enclaves hosted in  
4  
5 817 pantelleritic magmas (Pantelleria, Italy): Implications for pantellerite petrogenesis. *Journal of*  
6  
7  
8 818 *Volcanology and Geothermal Research* **301**, 169-179.  
9  
10  
11 819 Lanzo, G., Landi, P. & Rotolo, S.G. (2013). Volatiles in pantellerite magmas: A case study of the  
12  
13 820 Green Tuff Plinian eruption (Island of Pantelleria). *Journal of Volcanology and Geothermal*  
14  
15 821 *Research* **262**, 153-163.  
16  
17  
18  
19 822 Le Maitre, R.W. (Ed.) (2002). A classification of igneous rocks and glossary of terms.  
20  
21 823 Recommendations of the International Union of Geological Sciences Subcommittee on the  
22  
23 824 Systematics of Igneous Rocks. Second Edition. Cambridge University Press, Cambridge.  
24  
25  
26  
27 825 Lowenstern, J.B. (1994). Chlorine, fluid immiscibility, and degassing in peralkaline magmas from  
28  
29 826 Pantelleria, Italy. *American Mineralogist* **79**, 353-369.  
30  
31  
32  
33 827 Lowenstern, J.B. & Mahood, G.A. (1991). New data on magmatic H<sub>2</sub>O contents of pantellerites, with  
34  
35 828 implications for petrogenesis and eruptive dynamics at Pantelleria. *Bulletin of Volcanology* **54**, 78-  
36  
37 829 83.  
38  
39  
40  
41 830 Macdonald, R. (1974). Nomenclature and petrochemistry of the peralkaline oversaturated extrusive  
42  
43 831 rocks. *Bulletin Volcanologique* **38**, 498-516.  
44  
45  
46  
47 832 Macdonald, R., Bagiński, B., Belkin, H.E., Dzierżanowski, P. & Jeżak, L. (2008).  
48  
49 833 Compositional variations in apatite from a benmoreite - peralkaline rhyolite volcanic suite,  
50  
51 834 Kenya Rift Valley. *Mineralogical Magazine* **72**, 1147-1161.  
52  
53  
54  
55

- 1  
2  
3 835 Macdonald, R., Bagiński, B., Leat, P.T, White, J.C. & Dzierzanowski, P. (2011). Mineral stability in  
4  
5 836 peralkaline silicic rocks: Information from trachytes of the Menengai volcano, Kenya. *Lithos* **125**,  
6  
7  
8 837 553-568.  
9  
10  
11 838 Macdonald, R., Bagiński, B., Ronga, F., Dzierzanowski, P., Lustrino, M., Marzoli, A. & Melluso, L.  
12  
13 839 (2012). Evidence for extreme fractionation of peralkaline silicic magmas, the Boseti volcanic  
14  
15 840 complex, Main Ethiopian Rift. *Mineralogy and Petrology* **104**, 163-175.  
16  
17  
18 841 Macdonald, R., Navarro, J.M., Upton, B.G.J. & Davies, G.R. (1994). Strong compositional zonation in  
19  
20 842 peralkaline magma: Menengai, Kenya Rift Valley. *Journal of Volcanology and Geothermal*  
21  
22 843 *Research* **60**, 301-325.  
23  
24  
25 844 Mahood, G.A. (1984). Pyroclastic rocks and calderas associated with strongly peralkaline magmatism.  
26  
27 845 *Journal of Geophysical Research* **89**, 8540-8552.  
28  
29  
30 846 Mahood, G.A. & Baker, D.R. (1986). Experimental constraints on depths of fractionation of mildly  
31  
32 847 alkalic basalts and associated felsic rocks: Pantelleria, Strait of Sicily. *Contributions to Mineralogy*  
33  
34 848 *and Petrology* **93**, 251-264.  
35  
36  
37  
38 849 Mahood, G.A. & Hildreth, W. (1986). Geology of the peralkaline volcano at Pantelleria, Strait  
39  
40 850 of Sicily. *Bulletin of Volcanology* **48**, 143-172.  
41  
42  
43  
44 851 Mahood, G.A. & Stimac, J.A. (1990). Trace-element partitioning in pantellerites and  
45  
46 852 trachytes. *Geochimica et Cosmochimica Acta* **54**, 2257-2276.  
47  
48  
49  
50 853 Margari, V., Pyle, D.M., Bryant, C. & Gibbard, P.L. (2007). Mediterranean tephra  
51  
52 854 stratigraphy revisited: results from a long terrestrial sequence on Lesvos Island, Greece.  
53  
54  
55

- 1  
2  
3 855 *Journal of Volcanology and Geothermal Research* **163**, 34-54.  
4  
5  
6 856 Mattia, M., Bonaccorso, A. & Guglielmino, F. (2007). Ground deformations in the Island of  
7  
8 857 Pantelleria (Italy): Insights into the dynamics of the current intereruptive period. *Journal of*  
9  
10  
11 858 *Geophysical Research* **112**, B11406.  
12  
13  
14 859 Morelli, C., Gantar, C. & Pisani, M. (1975). Bathymetry, gravity and magnetism in the Straits  
15  
16  
17 860 of Sicily and Ionian Sea. *Bolletino di Geofisica Teorica ed Applicata* **17**, 39-58.  
18  
19  
20 861 Mungall, J.E. & Martin, R.F. (1995). Petrogenesis of basalt-comendite and basalt-pantellerite  
21  
22  
23 862 suites, Terceira, Azores, and some implications for the origin of ocean-island rhyolites.  
24  
25  
26 863 *Contributions to Mineralogy and Petrology* **119**, 43-55.  
27  
28  
29 864 Neave, D.A., Fabbro, G., Herd, R.A., Petrone, C.M. & Edmonds, M. (2012). Melting,  
30  
31  
32 865 differentiation and degassing at the Pantelleria volcano, Italy. *Journal of Petrology* **53**, 637-  
33  
34  
35 866 663.  
36  
37  
38 867 Noble, D.C. (1967). Sodium, potassium, and ferrous iron contents of some secondarily  
39  
40  
41 868 hydrated natural silicic glasses. *American Mineralogist* **52**, 280-286.  
42  
43  
44 869 Noble, D.C. (1970). Loss of sodium from crystallized comendite welded tuffs of the Miocene  
45  
46  
47 870 Grouse Canyon Member of the Belted Range Tuff, Nevada. *Geological Society of America*  
48  
49  
50 871 *Bulletin* **81**, 2677-2687.  
51  
52  
53 872 Noble, D.C., Smith, V.C. & Peck, L.C. (1967). Loss of halogens from crystallized and glassy  
54  
55

- 1  
2  
3 873 silicic volcanic rocks. *Geochimica et Cosmochimica Acta* **31**, 215-223.  
4  
5  
6 874 Orsi, G. & Sheridan, M.F. (1984). The Green Tuff of Pantelleria: rheoignimbrite or  
7  
8 875 rheomorphic fall? *Bulletin of Volcanology* **47**, 611-626.  
9  
10  
11 876 Orsi, G., Gallo, G. & Zanchi, A. (1991). Simple-shearing block resurgence in caldera  
12  
13  
14 877 depressions. A model from Pantelleria and Ischia. *Journal of Volcanology and Geothermal*  
15  
16  
17 878 *Research* **47**, 1-11.  
18  
19  
20 879 Pimentel, A., Zanon, V., de Groot, L.V., Hipólito, A., Di Chiara, A. & Self, S. (2016). Stress-  
21  
22  
23 880 induced comenditic trachyte effusion triggered by trachybasalt intrusion: multidisciplinary  
24  
25  
26 881 study of the AD 1761 eruption at Terceira Island (Azores). *Bulletin of Volcanology* **78**, 22.  
27  
28  
29 882 Pouchou, J.L. & Pichoir, J.F. (1991). Quantitative analysis of homogeneous or stratified  
30  
31  
32 883 microvolumes applying the model 'PAP'. In: Heinrich, K.F.J. & Newbury, D.E. (eds)  
33  
34  
35 884 *Electron Probe Quantification*. Plenum Press, New York, 31-75.  
36  
37  
38 885 Prosperini, N., Perugini, D., Poli, G. & Manetti, P. (1990). Magmatic enclaves distribution  
39  
40  
41 886 within the Khaggiar lava dome (Pantelleria, Italy): implications for magma chamber  
42  
43  
44 887 dynamics and eruption. *Acta Vulcanologica* **12**, 37-47.  
45  
46  
47 888 Putirka, K.D., Mikaelian, H., Ryerson, F. & Shaw, H. (2003). New clinopyroxene-liquid  
48  
49  
50 889 thermobarometers for mafic, evolved, and volatile-bearing lava compositions, with  
51  
52  
53 890 applications to lavas from Tibet and the Snake River Plain, Idaho. *American Mineralogist*  
54  
55

- 1  
2  
3 891 **88**, 1542-1554.
- 4  
5  
6 892 Romano, P., Andújar, J., Scaillet, B., Romengo, N., di Carlo, I. & Rotolo, S.G. (2018).
- 7  
8 893 Phase equilibria of Pantelleria trachytes (Italy): constraints on pre-eruptive conditions and
- 9  
10  
11 894 on the metaluminous to peralkaline transition in silicic magmas. *Journal of Petrology* **59**,
- 12  
13  
14 895 559-588.
- 15  
16  
17 896 Romano, P., White, J.C., Ciulla, A., Di Carlo, I., D’Oriano, C.D., Landi, P. & Rotolo, S.G.
- 18  
19  
20 897 (submitted). Volatile and trace element content in melt inclusions from the zoned Green
- 21  
22  
23 898 Tuff ignimbrite (Pantelleria, Sicily): petrological inferences. Submitted to *Annals of*
- 24  
25  
26 899 *Geophysics*.
- 27  
28  
29 900 Romengo, N., Landi, P. & Rotolo, S.G. (2012). Evidence of basaltic magma intrusions in a
- 30  
31  
32 901 trachytic magma chamber at Pantelleria (Italy). *Periodico di Mineralogia* **81**, 163-178.
- 33  
34  
35 902 Sack, R.O., Carmichael, I.S.E., Rivers, M. & Ghiorso, M.S. (1980). Ferric-ferrous equilibria
- 36  
37  
38 903 in natural silicate liquids at 1 bar. *Contributions to Mineralogy and Petrology* **75**, 369-376.
- 39  
40  
41 904 Scaillet, B. & Macdonald, R. (2001). Phase relations of peralkaline silicic magmas and
- 42  
43  
44 905 petrogenetic implications. *Journal of Petrology* **42**, 825-845.
- 45  
46  
47 906 Scaillet, B. & Macdonald, R. (2003). Experimental constraints on the relationships between
- 48  
49  
50 907 peralkaline rhyolites of the Kenya Rift Valley. *Journal of Petrology* **94**, 1867-1894.
- 51  
52  
53 908 Scaillet, B. & Macdonald, R. (2006). Experimental constraints on pre-eruptive conditions of
- 54  
55

- 1  
2  
3 909 pantelleritic magmas: Evidence from the Eburru complex, Kenya Rift. *Lithos* **91**, 95-108.  
4  
5  
6 910 Scaillet, B., Macdonald, R., Buccheri, V., Rotolo, S.G. & Pichavant, M. (2005). Phase  
7  
8 911 equilibrium constraints on the production and storage of peralkaline silicic magmas:  
9  
10  
11 912 insights from Kenya and Pantelleria. *Peralkaline rocks: Sources, economic potential and*  
12  
13  
14 913 *evolution from alkaline melts* (M. Marks, ed.). Workshop on peralkaline rocks, Tübingen,  
15  
16  
17 914 Germany.  
18  
19  
20 915 Scaillet, S., Rotolo, S.G., La Felice, S. & Vita-Scaillet, G. (2011). High-resolution  $^{40}\text{Ar}/^{39}\text{Ar}$   
21  
22  
23 916 chronostratigraphy of the post-caldera (<20 ka) volcanic activity at Pantelleria, Sicily  
24  
25  
26 917 Strait. *Earth and Planetary Science Letters* **309**, 280-290.  
27  
28  
29 918 Scaillet, S., Vita-Scaillet, G. & Rotolo, S.G. (2013). Millennial-scale phase relationships between ice-  
30  
31  
32 919 core and Mediterranean marine records: insights from high-precision  $^{40}\text{Ar}/^{39}\text{Ar}$  dating of the Green  
33  
34  
35 920 Tuff of Pantelleria, Sicily Strait. *Quaternary Science Reviews* **78**, 141-154.  
36  
37  
38 921 Schuraytz, B.C., Vogel, T.A. & Younker, L.W. (1989). Evidence for dynamic withdrawal from a  
39  
40  
41 922 layered magma body: The Topopah Spring Tuff, southwestern Nevada. *Journal of Geophysical*  
42  
43 923 *Research* **94**, 5925-5942.  
44  
45  
46 924 Spera, F.J., Yuen, D.A., Greer, J.C. & Sewell, G. (1986). Dynamics of magma withdrawal from  
47  
48 925 stratified magma chambers. *Geology* **14**, 723-726.  
49  
50  
51 926 Sumner, J.M. & Wolff, J. (2003). Petrogenesis of mixed-magma, high-grade, peralkaline ignimbrite  
52  
53  
54 927 'TL' (Gran Canaria): diverse styles of mixing in a replenished, zoned magma chamber. *Journal of*  
55  
56 41  
57  
58  
59  
60

- 1  
2  
3 928 *Volcanology and Geothermal Research* **126**, 109-126.
- 4  
5 929 Sun, S.-S. & McDonough, W.F. (1989). Chemical and isotopic systematics of oceanic basalts:  
6 930 implications for mantle composition and processes. *Magmatism in the Ocean Basins* (A.D.  
7 931 Saunders & M.J. Norry, eds.) *Geological Society Special Publication* **42**, 313-345.
- 8  
9  
10  
11 932 Troll, V.R. & Schmincke, H.-U. (2002). Magma mixing and crustal recycling recorded in ternary  
12  
13  
14 933 feldspar from compositionally zoned peralkaline ignimbrite 'A', Gran Canaria, Canary Islands.  
15  
16 934 *Journal of Petrology* **43**, 243-270.
- 17  
18  
19 935 Verzhbitsky, E.V. & Kononov, M.V. (2003). Heat flow and origin of the lithosphere in the central  
20  
21 936 Mediterranean region. *Geotectonics* **37**, 328-336.
- 22  
23  
24 937 Villari, L. (1974). The island of Pantelleria. *Bulletin of Volcanology* **38**, 680-724.
- 25  
26 938 Weaver, S.D., Gibson, I.L., Houghton, B.F. & Wilson, C.J.N. (1990). Mobility of rare earth  
27  
28 939 and other elements during crystallization of peralkaline silicic lavas. *Journal of*  
29  
30 940 *Volcanology and Geothermal Research* **43**, 57-70.
- 31  
32  
33  
34  
35  
36  
37 941 White, J.C., Holt, G.S., Parker, D.F. & Ren, M. (2003). Trace-element partitioning between  
38  
39 942 alkali feldspar and peralkalic quartz trachyte to rhyolite magma. Part 1: Systematics of  
40  
41 943 trace-element partitioning. *American Mineralogist* **88**, 316-329.
- 42  
43  
44  
45  
46 944 White, J.C., Ren, M. & Parker, D.F. (2005). Variation in mineralogy, temperature, and  
47  
48 945 oxygen fugacity in a suite of strongly peralkaline lavas and tuffs, Pantelleria, Italy. *The*  
49  
50 946 *Canadian Mineralogist* **43**, 1331-1347.
- 51  
52  
53  
54  
55

- 1  
2  
3 947 White, J.C., Parker, D.F. & Ren, M. (2009). The origin of trachyte and pantellerite from  
4  
5 948 Pantelleria, Italy: Insights from major element, trace element, and thermodynamic  
6  
7  
8 949 modelling. *Journal of Volcanology and Geothermal Research* **179**, 33-55.  
9  
10  
11 950 Williams, R., Branney, M.J. & Barry, T.L. (2014). Temporal and spatial evolution of a  
12  
13  
14 951 waxing then waning catastrophic density current revealed by chemical mapping. *Geology*  
15  
16  
17 952 **42**, 107-110.  
18  
19  
20 953 Wolff, J.A. & Wright, J.V. (1981). Formation of the Green Tuff, Pantelleria. *Bulletin of*  
21  
22  
23 954 *Volcanology* **44**, 681-690.  
24  
25  
26 955 Wright, J.V. (1980). Stratigraphy and geology of the welded air-fall tuffs of Pantelleria.  
27  
28  
29 956 *Geologisches Rundschau* **69**, 263-291.  
30  
31  
32 957  
33

34 **Figure captions**

35  
36 959

37  
38 960 **Figure 1.** Locality map showing the distribution of the Green Tuff ignimbrite and the rim  
39  
40 961 faults of the La Vecchia and Cinque Denti calderas. **Sample localities are marked.** Simplified  
41  
42 962 from Scaillet *et al.* (2011).  
43  
44

45 963

46  
47  
48 964 **Figure 2.** Vertical section through the Green Tuff pumice fall and ignimbrite at the type  
49  
50 965 locality on the Monastero scarp (Fig. 1) where it is ~7.5 m thick. Modified from Williams *et*  
51  
52 966 *al.* (2014). **The trachytic component is found in the rheomorphic vitrophyre at the top of the**  
53  
54  
55 967 **deposit (wavy lines). Approximate positions of our samples within the stratigraphy are shown.**

56 43  
57  
58  
59  
60

1  
2  
3 968

4 969 **Figure 3.** Resorption of phenocrysts in trachytic host rocks. (a) Sieve-texture in alkali  
5  
6 feldspar (Kfs). The small phenocryst is fayalite (Ol). Sample 150522. (b) Heavily resorbed  
7 970 alkali feldspar in 150513. Note the darkening and incipient devitrification of the glass (Gl)  
8  
9 971 around the crystal (arrowed). (c) Fayalite phenocryst (Ol), with apatite (Ap) inclusion. The  
10  
11 972 crystal partially includes a magnetite microphenocryst (Mag). Sample 150513. (d) Partially  
12  
13 973 resorbed hedenbergite phenocryst (Cpx: 150513), containing inclusions of apatite and  
14  
15 974 magnetite. The associated phenocryst is fayalite, completely replaced by magnetite + quartz.  
16  
17 975 Note the darkening and incipient devitrification of the glass around the crystal. Details of the  
18  
19 976 samples are given in the Appendix.  
20  
21 977  
22  
23  
24

25 978

26  
27  
28 979 **Figure 4.** Different styles of magma mixing in the Green Tuff. Samples: (a) Round blebs of  
29  
30 980 dark glass embedded in pale brown glass. Alkali feldspar crystals (Kfs) occur in both types.  
31  
32 981 Sample 150513. (b) Densely welded tuff with intermingled dark brown and pale fiamme.  
33  
34 982 Sample 150551. (c) Densely welded type with mingling of at least two varieties of glass.  
35  
36 983 Sample 150543. (d) A less densely welded sample shows pale and slightly deeper brown  
37  
38 984 glasses streakily intermingled along their junction. A euhedral aenigmatite phenocryst is  
39  
40 985 marked (Aen). Sample 150544. Details of the samples are given in the Appendix.  
41  
42  
43

44 986

45  
46  
47 987 **Figure 5.** (Si + Na) plotted against (Al + Ca) for aenigmatite phenocrysts in the Green Tuff.  
48  
49 988 **New data from this paper, Electronic Appendix 2 (a); literature data from Mahood & Stimac**  
50  
51 989 **(1990), White *et al.* (2009) and Neave *et al.* (2012).**  
52  
53

54 990

55  
56 44  
57  
58  
59  
60

1  
2  
3  
4  
5  
6  
7  
8  
9  
10  
11  
12  
13  
14  
15  
16  
17  
18  
19  
20  
21  
22  
23  
24  
25  
26  
27  
28  
29  
30  
31  
32  
33  
34  
35  
36  
37  
38  
39  
40  
41  
42  
43  
44  
45  
46  
47  
48  
49  
50  
51  
52  
53  
54  
55  
56  
57  
58  
59  
60

991 **Figure 6.** Plots of the FK/A index ( $\text{mol}(\text{FeO}^*+\text{K}_2\text{O})/\text{Al}_2\text{O}_3$ ) versus the peralkalinity index  
992 (P.I. =  $\text{mol}(\text{Na}_2\text{O}+\text{K}_2\text{O})/\text{Al}_2\text{O}_3$ ) to test for potential sodium loss in peralkaline rocks (White *et*  
993 *al.*, 2003). (a) Whole-rock compositions, with potentially altered samples labelled. **Data from**  
994 **Table 2. (b) Glass analyses in individual samples (listed). Data from Electronic Appendix 3.**  
995

996 **Figure 7.** Whole-rocks (WR) and **glass (all symbols except + and x)** for Green Tuff plotted in  
997 the classification scheme for peralkaline silicic rocks of Macdonald (1974). **CT, comenditic**  
998 **trachyte; C, comendite; PT, pantelleritic trachyte; P, pantellerite.** TS – analyses for **whole-**  
999 **rocks** from the type section of the Green Tuff from Williams *et al.* (2014). **Trends 1 to 3**  
1000 **reflect changing fractionating assemblages; see text for details.** The trend marked Di Carlo is  
1001 for experimental glasses in the study of a Pantescan pantellerite by Di Carlo *et al.* (2010).  
1002 Data sources: whole rocks (WR) – Table 2, this paper, Mahood & Stimac (1990), White *et al.*  
1003 (2009); glass – this paper, Electronic Appendix 3, Mahood & Stimac (1990; **samples 7, 226**  
1004 **and 231/233) and Neave *et al.* (2012; sample 09PNL033).**

1006 **Figure 8.** (a) Selected major element v.  $\text{SiO}_2$  plots for Green Tuff whole-rocks. **The ranges of**  
1007 **glass analyses are shown as fields.** (b) Selected trace element v.  $\text{SiO}_2$  plots. **Data from this**  
1008 **paper, Table 2, Electronic Appendix 3, and White *et al.* (2009, samples 060537 and 060545).**  
1009 The arrowed sample (150541) in the  $\text{Al}_2\text{O}_3$  and Ba plots is thought to be slightly feldspar-  
1010 accumultic. Also shown in both plots are whole-rock analyses of trachytes from Montagna  
1011 Grande and Monte Gibebe (data from Villari (1974), Mahood & Hildreth (1986), Avanzinelli  
1012 *et al.* (2004), Ferla & Meli (2006) and White *et al.* (2009)). The field for MgO in glass has  
1013 been drawn omitting two anomalously high analyses.

1  
2  
3 1014

4 1015 **Figure 9.** Chondrite-normalized REE plots for (a) whole-rocks and (b) glasses. Normalizing  
5 1016 factors from Sun & McDonough (1989). Data sources: whole-rocks, this paper, Table 2, and  
6 1017 Mahood & Stimac (1990, sample 231); glass, patterns 3 and 5, Mahood & Stimac (1990;  
7 1018 samples 226 and 231), pattern 2, Neave *et al.* (2012; sample 09PNL033) and patterns 1 and 4,  
8 1019 Williams *et al.* (2014; samples 44E and 44H). Glass patterns 4 and 5 are comenditic trachyte,  
9 1020 patterns 1, 2 and 3 are pantelleritic.

10  
11  
12  
13  
14  
15  
16  
17  
18 1021

19  
20  
21 1022 **Figure 10.** Examples of different styles of magma mixing in the Green Tuff. Values are for  
22 1023 SiO<sub>2</sub> wt %. (a) Streaky intermingling of glass ranging in composition from ~67 to 71 wt %  
23 1024 SiO<sub>2</sub>. Sample 150551. (b) Fragment of pale brown glass in very dark brown host. Sample  
24 1025 150521. (c) The composition of the pale glass in (b) ranges from 66 to 73 wt % SiO<sub>2</sub>.

25  
26  
27  
28  
29  
30  
31 1026

32  
33  
34 1027 **Figure 11.** (a) Comparison of calculated temperatures (°C) for whole-rock compositions and  
35 1028 assemblages plotted against Zr concentration. QUILF95 points are calculated from olivine-  
36 1029 clinopyroxene equilibria (Andersen *et al.*, 1993). CPX-WR are calculated from clinopyroxene-whole  
37 1030 rock compositions (Putirka *et al.*, 2003). KFS were determined from the position of the whole rock  
38 1031 composition in Fig. 12 (see text for details). (b) Comparison of calculated temperatures for glass  
39 1032 compositions plotted against Zr concentration, determined with the techniques described for (a).  
40 1033 Averages with error bars are plotted for CPX and individual points are plotted for KFS to facilitate  
41 1034 readability.

42  
43  
44  
45  
46  
47  
48  
49  
50 1035

1  
2  
3 1036 **Figure 12.** (a) Whole-rock and (b) glass analyses plotted in the system Q-Ab-Or-H<sub>2</sub>O with 8.3 mol%  
4  
5 1037 aegirine + 8.3 mol% sodium metasilicate added and P<sub>H<sub>2</sub>O</sub> = 1000 bar. (Carmichael & MacKenzie,  
6  
7 1038 1963). Whole rock analyses displayed include those presented in this study (Table 2) and from the  
8  
9 1039 literature (Civetta *et al.*, 1984, 1989; Kovalenko *et al.*, 1994; Esperança & Crisci, 1995; Avanzinelli *et*  
10  
11 1040 *al.*, 2004; Ferla & Meli, 2006; White *et al.*, 2009; Williams *et al.*, 2014). The crosses mark the alkali  
12  
13 1041 feldspar liquidus surface.

14  
15  
16 1042

17  
18 1043 **Figure 13.** (a) Silica activity ( $a_{\text{SiO}_2}$ ) relative to quartz saturation and (b) oxygen fugacity relative to  
19  
20 1044 the FMQ buffer plotted against temperature. W09-GT and W-09-TR are the results of QUILF95  
21  
22 1045 geothermobarometry for the Green Tuff and Montagna Grande Trachyte, respectively, from White *et*  
23  
24 1046 *al.* (2009). The fayalite-ilmenite-aenigmatite stability curve for  $X_{\text{Ilm}} = 0.95$  is calculated following  
25  
26 1047 Macdonald *et al.* (2011), with ilmenite activities calculated with the solution model of Andersen &  
27  
28 1048 Lindsley (1988).  $\Delta\text{FMQ} = \log f_{\text{O}_2} - \text{FMQ(T)}$ , with FMQ(T) calculated following Frost *et al.* (1988).  
29  
30 1049 (c) The experimental results of Scaillet & Macdonald (2006) for Eburru and Di Carlo *et al.* (2010) for  
31  
32 1050 Pantelleria show the strong positive correlation between oxygen fugacity (as  $\Delta\text{FMQ}$ ) and melt water  
33  
34 1051 content (wt % H<sub>2</sub>O<sub>melt</sub>).

35  
36  
37 1052

38  
39  
40 1053 **Figure 14.** Eu/Eu\* plotted against Zr content for Green Tuff samples. Data sources: whole-  
41  
42 1054 rocks – this paper, Table 2; Mahood & Stimac (1990); White *et al.* (2009); glass – Mahood &  
43  
44 1055 Stimac (1990, samples 7, 226, 231/233), Neave *et al.* (2012, sample 09PNL033), Williams *et*  
45  
46 1056 *al.* (2014, samples 44H and 44I).

47  
48  
49 1057

50  
51  
52 1058 **Figure 15.** Anhydrous melt densities, calculated by the method of Bottinga & Weill (1970), plotted  
53  
54 1059 against Zr contents for whole-rocks (open circles) and glasses (closed circles). The densities initially

55  
56 47

1  
2  
3 1060 decrease to Zr ~1500 ppm and then change little with increasing Zr. Data sources: this paper, Table 2  
4 and Electronic Appendix 3.  
5  
6

7  
8 1062  
9

10 1063 **Figure 16.** Maximum Zr content in glass in each Green Tuff whole-rock plotted against range  
11 of Zr contents in glass of same rock. The ranges indicate mixing in varying proportions of  
12 trachytic and rhyolitic melts. Also shown is the composition of a Montagna Grande glass,  
13  
14 1065 from Mahood & Stimac (1990, sample 119); its relative compositional similarity to the  
15  
16 1066 Montagna Grande whole-rocks suggests that the range of glasses in each sample must be  
17  
18 1067 small. Montagna Grande whole-rock data from Mahood & Stimac (1990), Avanzinelli *et al.*  
19  
20 1068 (2004), Ferla & Meli (2006) and White *et al.* (2009).  
21  
22 1069  
23  
24  
25

26 1070  
27  
28

29 1071 **Figure 17.** Possible relationships in the magmatic plumbing system prior to eruption of the  
30  
31 1072 Green Tuff. The crustal structure is from Civile *et al.* (1988).  
32  
33  
34  
35  
36  
37  
38  
39  
40  
41  
42  
43  
44  
45  
46  
47  
48  
49  
50  
51  
52  
53  
54  
55

1  
2  
3  
4  
5  
6  
7  
8  
9  
10  
11  
12  
13  
14  
15  
16  
17  
18  
19  
20  
21  
22  
23  
24  
25  
26  
27  
28  
29  
30  
31  
32  
33  
34  
35  
36  
37  
38  
39  
40  
41  
42  
43  
44  
45  
46  
47  
48  
49  
50  
51  
52  
53  
54  
55  
56  
57  
58  
59  
60

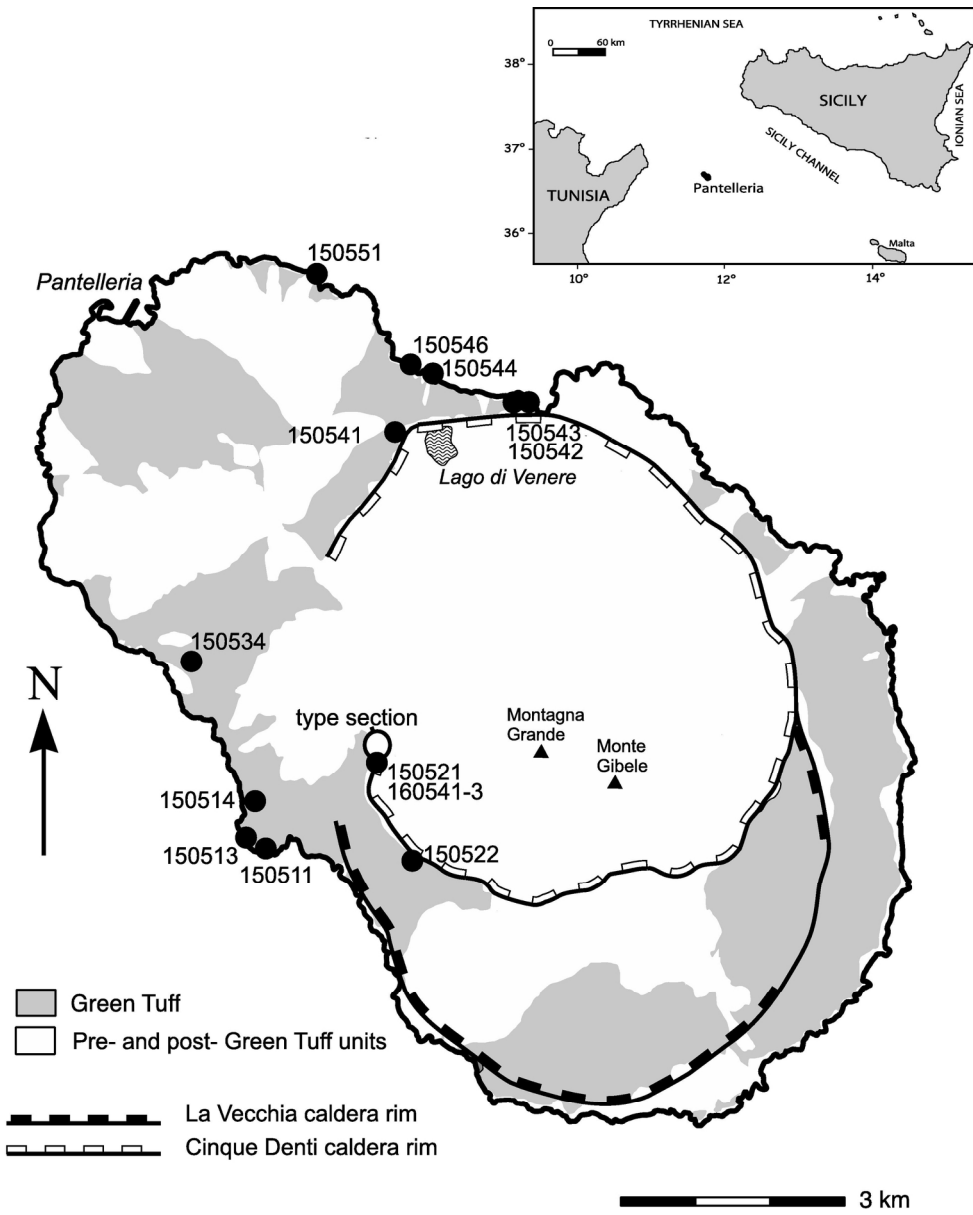


Figure 1. Locality map showing the distribution of the Green Tuff ignimbrite and the rim faults of the La Vecchia and Cinque Denti calderas. Sample localities are marked. Simplified from Scaillet et al. (2011).

166x204mm (300 x 300 DPI)

1  
2  
3  
4  
5  
6  
7  
8  
9  
10  
11  
12  
13  
14  
15  
16  
17  
18  
19  
20  
21  
22  
23  
24  
25  
26  
27  
28  
29  
30  
31  
32  
33  
34  
35  
36  
37  
38  
39  
40  
41  
42  
43  
44  
45  
46  
47  
48  
49  
50  
51  
52  
53  
54  
55  
56  
57  
58  
59  
60

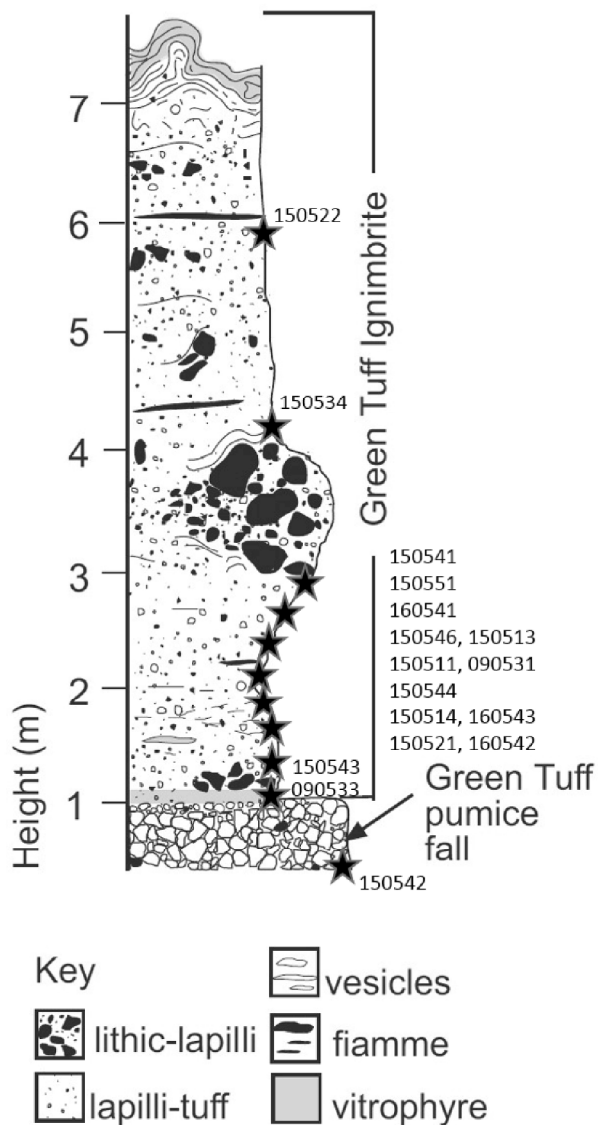


Figure 2. Vertical section through the Green Tuff pumice fall and ignimbrite at the type locality on the Monastero scarp (Fig. 1) where it is ~7.5 m thick. Modified from Williams et al. (2014). The trachytic component is found in the rheomorphic vitrophyre at the top of the deposit (wavy lines). Approximate positions of our samples within the stratigraphy are shown.

190x340mm (300 x 300 DPI)

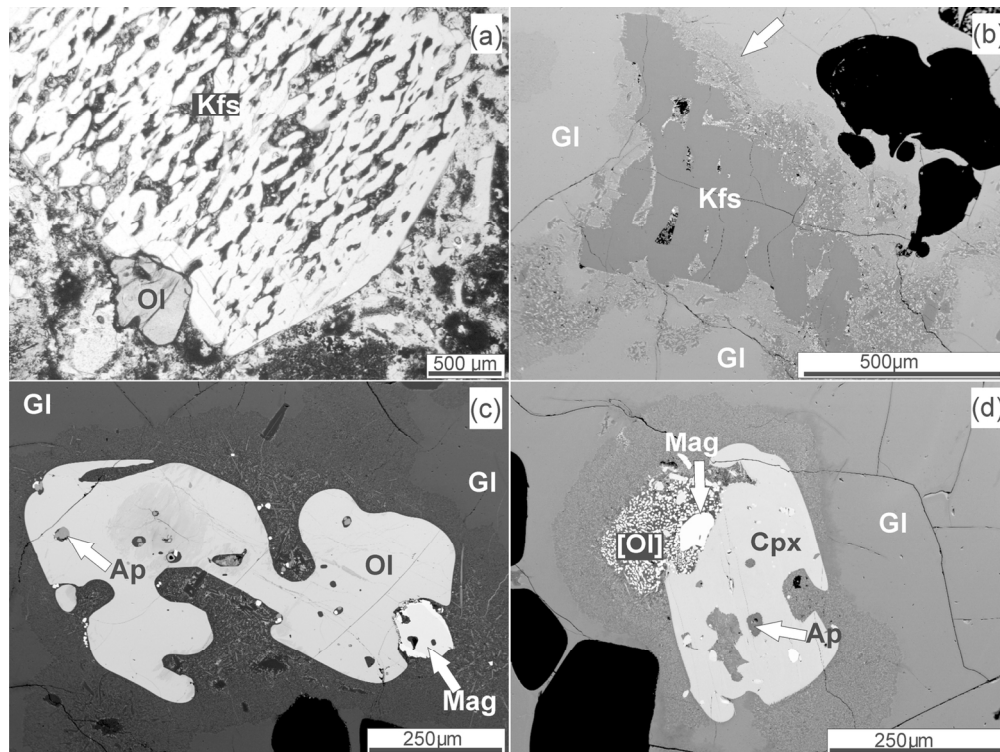


Figure 3. Resorption of phenocrysts in trachytic host rocks. (a) Sieve-texture in alkali feldspar (Kfs). The small phenocryst is fayalite (Ol). Sample 150522. (b) Heavily resorbed alkali feldspar in 150513. Note the darkening and incipient devitrification of the glass (Gl) around the crystal (arrowed). (c) Fayalite phenocryst (Ol), with apatite (Ap) inclusion. The crystal partially includes a magnetite microphenocryst (Mag). Sample 150513. (d) Partially resorbed hedenbergite phenocryst (Cpx: 150513), containing inclusions of apatite and magnetite. The associated phenocryst is fayalite, completely replaced by magnetite + quartz. Note the darkening and incipient devitrification of the glass around the crystal. Details of the samples are given in the Appendix.

134x100mm (300 x 300 DPI)

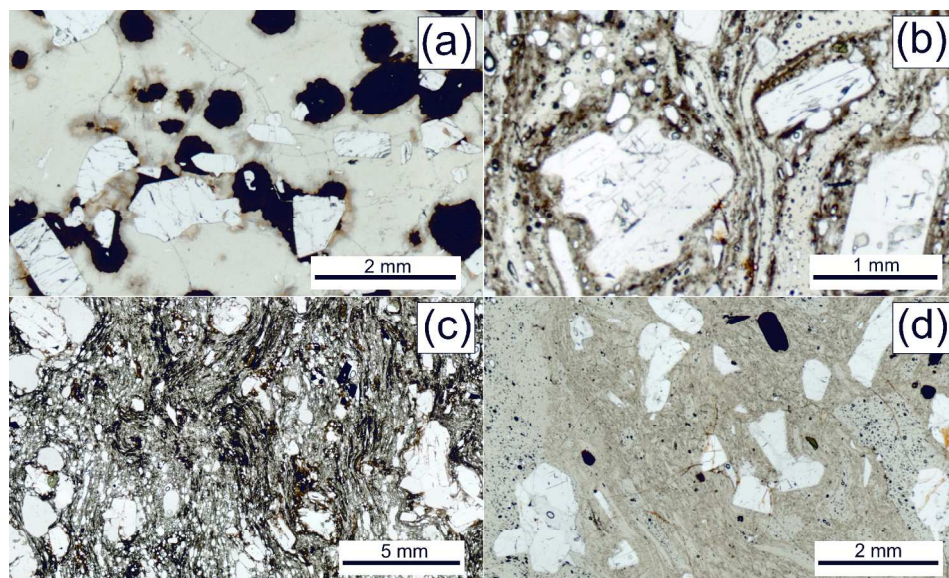


Figure 4. Different styles of magma mixing in the Green Tuff. Samples: (a) Round blebs of dark glass embedded in pale brown glass. Alkali feldspar crystals (Kfs) occur in both types. Sample 150513. (b) Densely welded tuff with intermingled dark brown and pale fiamme. Sample 150551. (c) Densely welded type with mingling of at least two varieties of glass. Sample 150543. (d) A less densely welded sample shows pale and slightly deeper brown glasses streakily intermingled along their junction. A euhedral aenigmatite phenocryst is marked (Aen). Sample 150544. Details of the samples are given in the Appendix.

186x116mm (300 x 300 DPI)

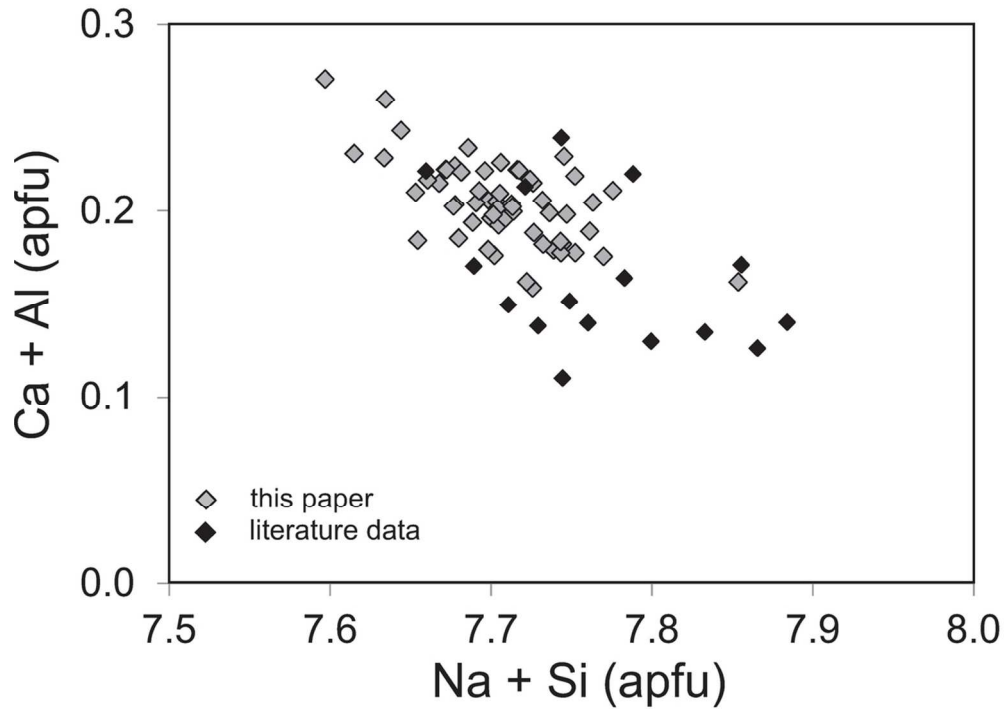


Figure 5. (Si + Na) plotted against (Al + Ca) for aenigmatite phenocrysts in the Green Tuff. New data from this paper, Electronic Appendix 2 (a); literature data from Mahood & Stimac (1990), White et al. (2009) and Neave et al. (2012).

107x75mm (300 x 300 DPI)

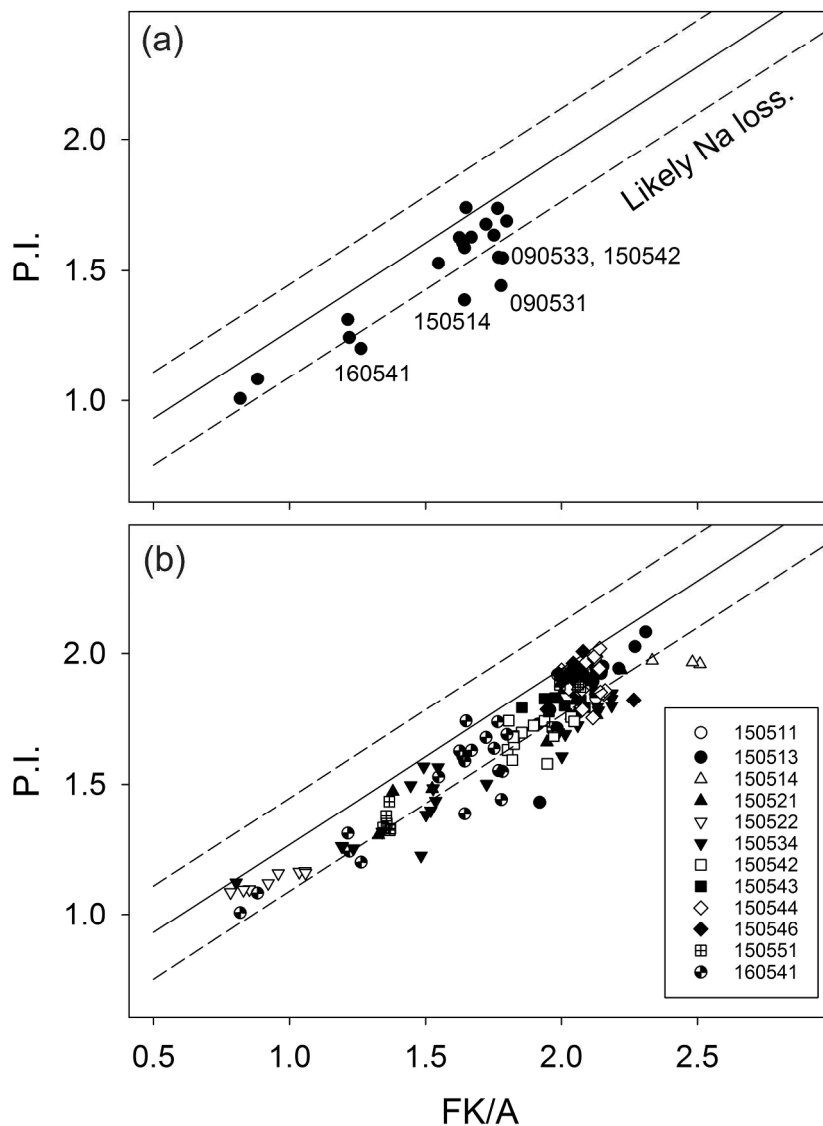


Figure 6. Plots of the FK/A index (mol (FeO\*+K<sub>2</sub>O)/Al<sub>2</sub>O<sub>3</sub>) versus the peralkalinity index (P.I. = mol (Na<sub>2</sub>O+K<sub>2</sub>O)/Al<sub>2</sub>O<sub>3</sub>) to test for potential sodium loss in peralkaline rocks (White et al., 2003). (a) Whole-rock compositions, with potentially altered samples labelled. Data from Table 2. (b) Glass analyses in individual samples (listed). Data from Electronic Appendix 3.

216x289mm (300 x 300 DPI)

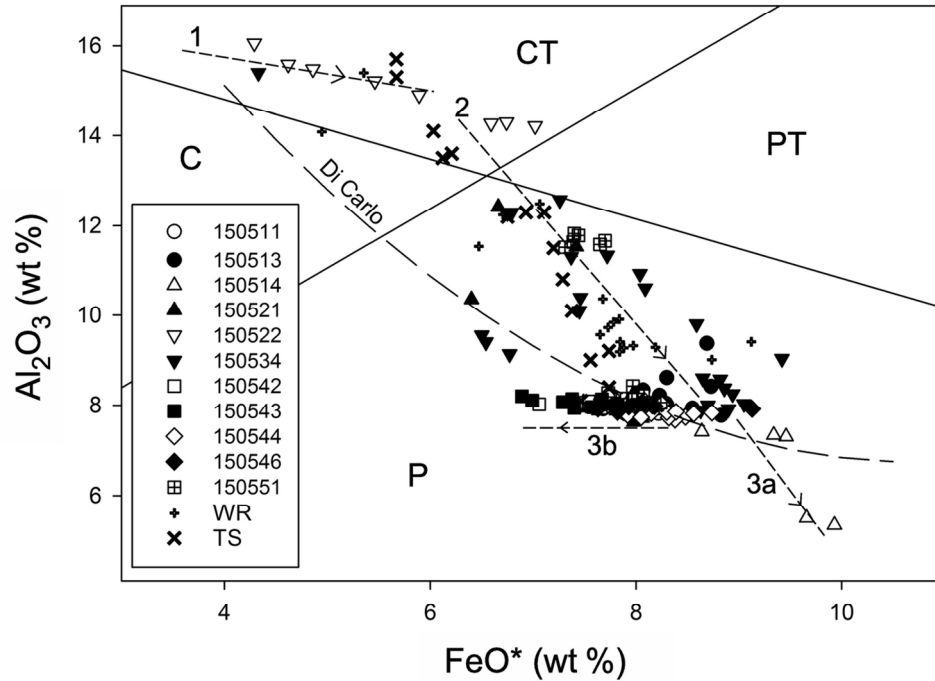


Figure 7. Whole-rocks (WR) and glass (all symbols except + and x) for Green Tuff plotted in the classification scheme for peralkaline silicic rocks of Macdonald (1974). CT, comenditic trachyte; C, comendite; PT, pantelleritic trachyte; P, pantellerite. TS – analyses for whole-rocks from the type section of the Green Tuff from Williams et al. (2014). Trends 1 to 3 reflect changing fractionating assemblages; see text for details. The trend marked Di Carlo is for experimental glasses in the study of a Pantescan pantellerite by Di Carlo et al. (2010). Data sources: whole rocks (WR) – Table 2, this paper, Mahood & Stimac (1990), White et al. (2009); glass – this paper, Electronic Appendix 3, Mahood & Stimac (1990; samples 7, 226 and 231/233) and Neave et al. (2012; sample 09PNL033).

121x95mm (300 x 300 DPI)

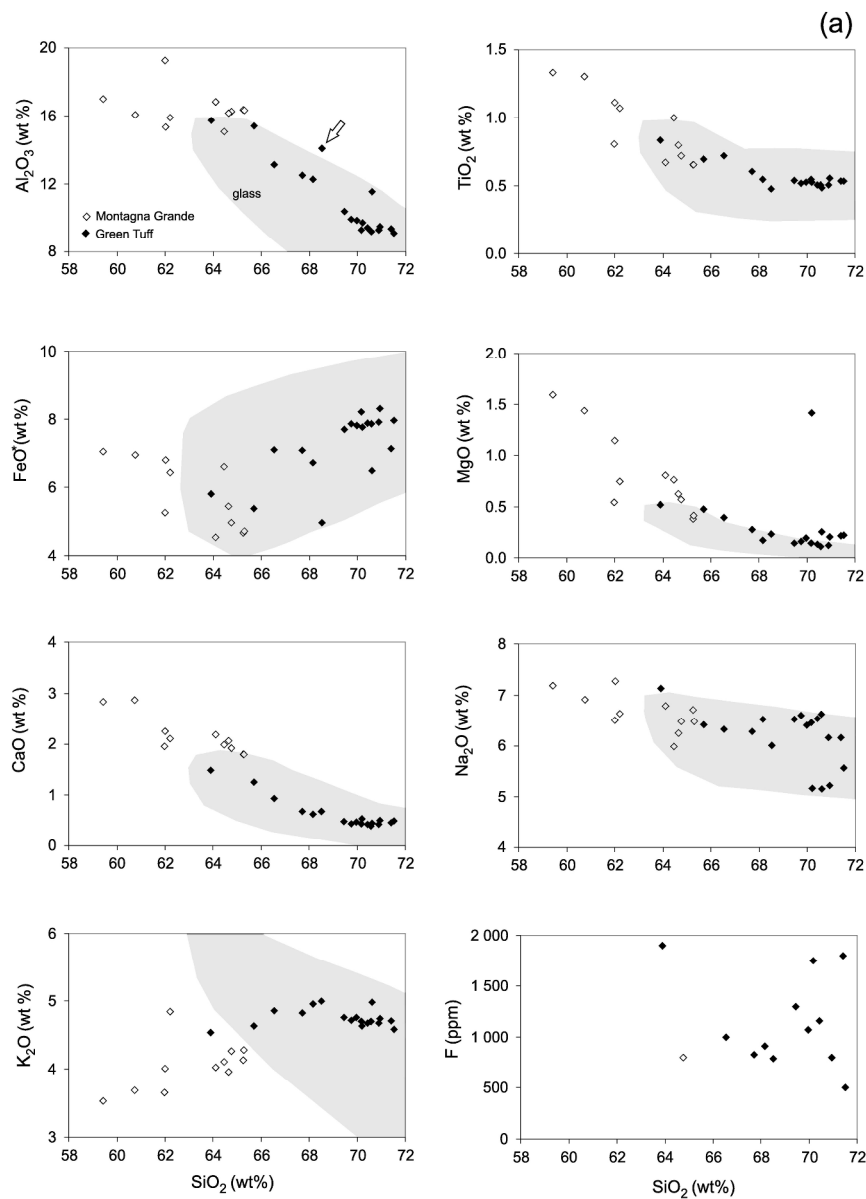


Figure 8. (a) Selected major element v.  $\text{SiO}_2$  plots for Green Tuff whole-rocks. The ranges of glass analyses are shown as fields. (b) Selected trace element v.  $\text{SiO}_2$  plots. Data from this paper, Table 2, Electronic Appendix 3, and White et al. (2009, samples 060537 and 060545). The arrowed sample (150541) in the  $\text{Al}_2\text{O}_3$  and Ba plots is thought to be slightly feldspar-accumulitic. Also shown in both plots are whole-rock analyses of trachytes from Montagna Grande and Monte Gibele (data from Villari (1974), Mahood & Hildreth (1986), Avanzinelli et al. (2004), Ferla & Meli (2006) and White et al. (2009)). The field for MgO in glass has been drawn omitting two anomalously high analyses.

276x371mm (300 x 300 DPI)

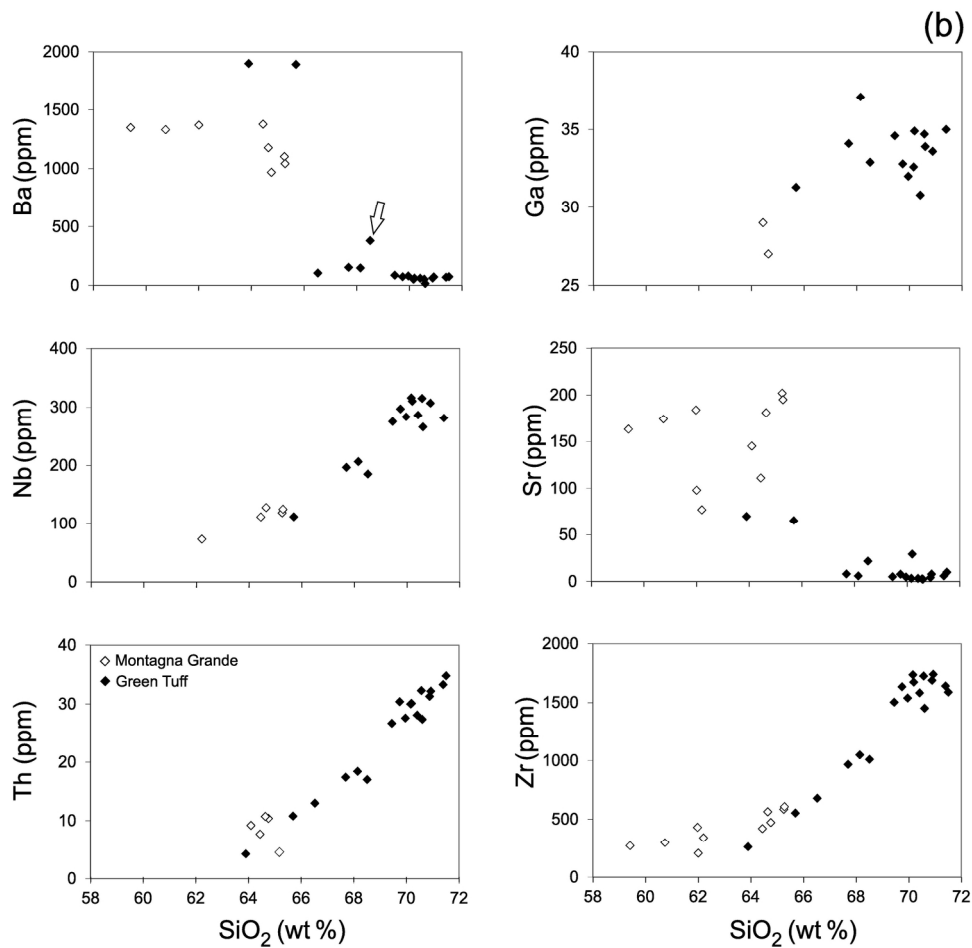


Figure 8. (a) Selected major element v. SiO<sub>2</sub> plots for Green Tuff whole-rocks. The ranges of glass analyses are shown as fields. (b) Selected trace element v. SiO<sub>2</sub> plots. Data from this paper, Table 2, Electronic Appendix 3, and White et al. (2009, samples 060537 and 060545). The arrowed sample (150541) in the Al<sub>2</sub>O<sub>3</sub> and Ba plots is thought to be slightly feldspar-accumulitic. Also shown in both plots are whole-rock analyses of trachytes from Montagna Grande and Monte Gibeale (data from Villari (1974), Mahood & Hildreth (1986), Avanzinelli et al. (2004), Ferla & Meli (2006) and White et al. (2009)). The field for MgO in glass has been drawn omitting two anomalously high analyses.

178x170mm (300 x 300 DPI)

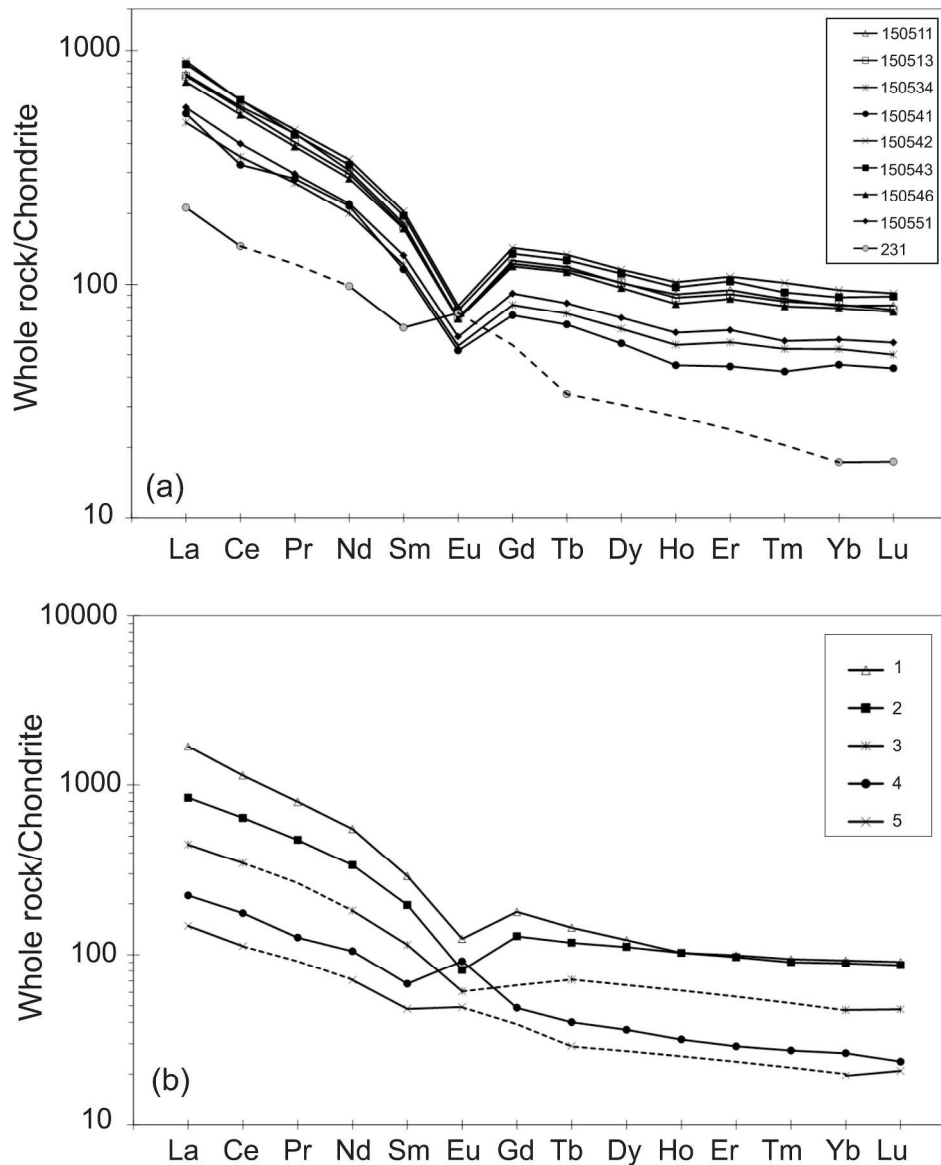


Figure 9. Chondrite-normalized REE plots for (a) whole-rocks and (b) glasses. Normalizing factors from Sun & McDonough (1989). Data sources: whole-rocks, this paper, Table 2, and Mahood & Stimac (1990, sample 231); glass, patterns 3 and 5, Mahood & Stimac (1990; samples 226 and 231), pattern 2, Neave et al. (2012; sample 09PNL033) and patterns 1 and 4, Williams et al. (2014; samples 44E and 44H). Glass patterns 4 and 5 are comenditic trachyte, patterns 1, 2 and 3 are pantelleritic.

238x299mm (300 x 300 DPI)

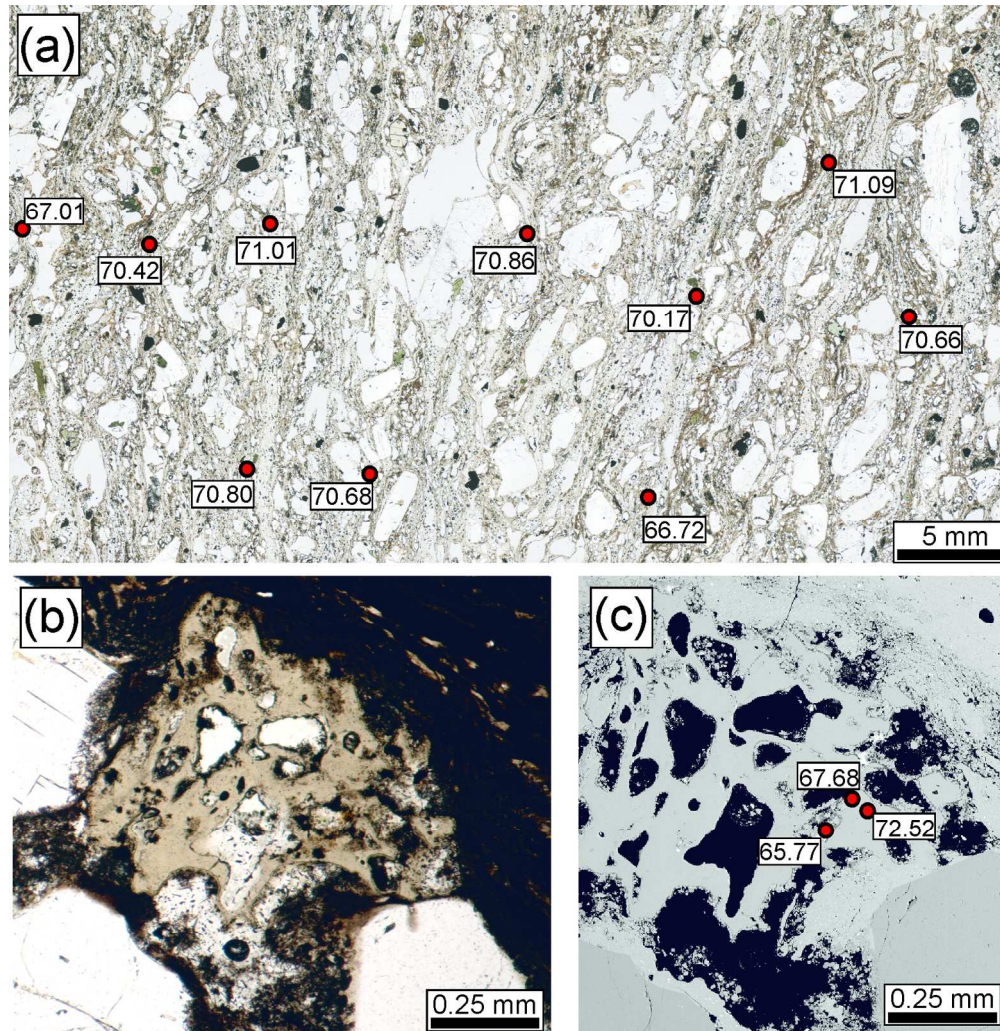


Figure 10. Examples of different styles of magma mixing in the Green Tuff. Values are for SiO<sub>2</sub> wt %. (a) Streaky intermingling of glass ranging in composition from ~67 to 71 wt % SiO<sub>2</sub>. Sample 150551. (b) Fragment of pale brown glass in very dark brown host. Sample 150521. (c) The composition of the pale glass in (b) ranges from 66 to 73 wt % SiO<sub>2</sub>.

157x162mm (300 x 300 DPI)

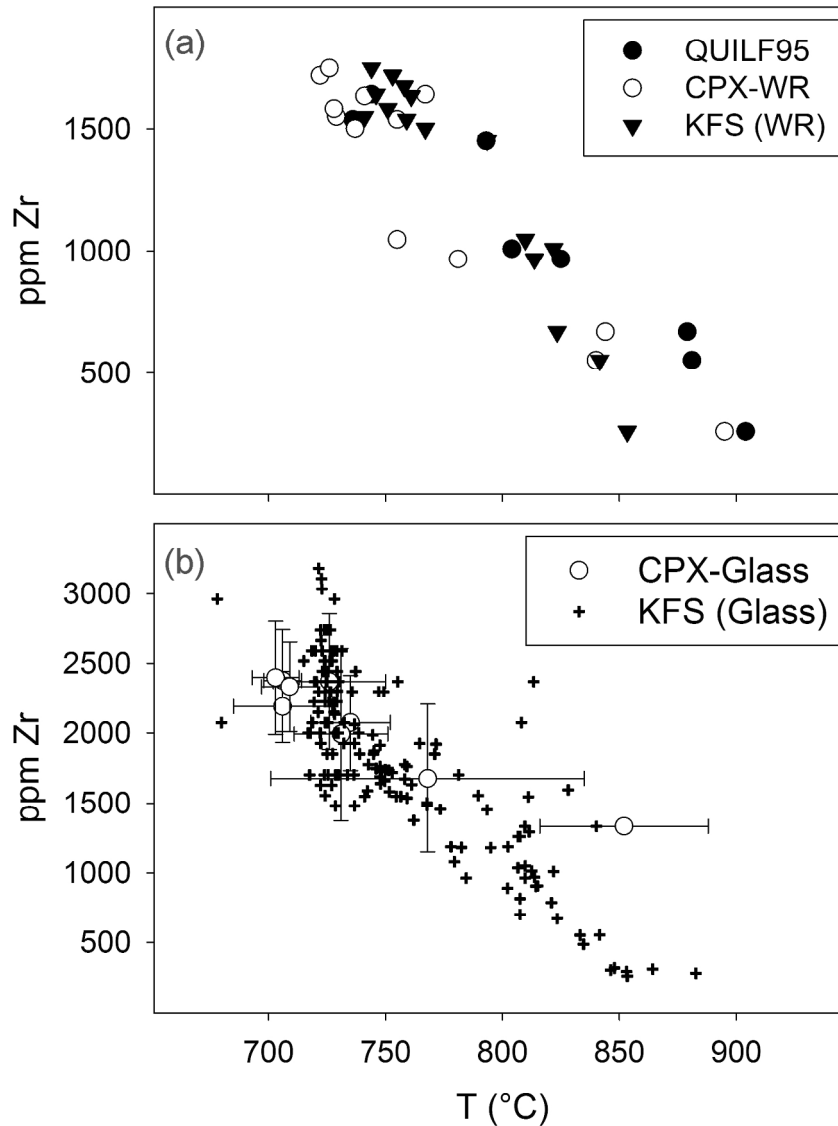


Figure 11. (a) Comparison of calculated temperatures ( $^{\circ}\text{C}$ ) for whole-rock compositions and assemblages plotted against Zr concentration. QUILF95 points are calculated from olivine-clinopyroxene equilibria (Andersen et al., 1993). CPX-WR are calculated from clinopyroxene-whole rock compositions (Putirka et al., 2003). KFS were determined from the position of the whole rock composition in Fig. 12 (see text for details). (b) Comparison of calculated temperatures for glass compositions plotted against Zr concentration, determined with the techniques described for (a). Averages with error bars are plotted for CPX and individual points are plotted for KFS to facilitate readability.

167x218mm (300 x 300 DPI)

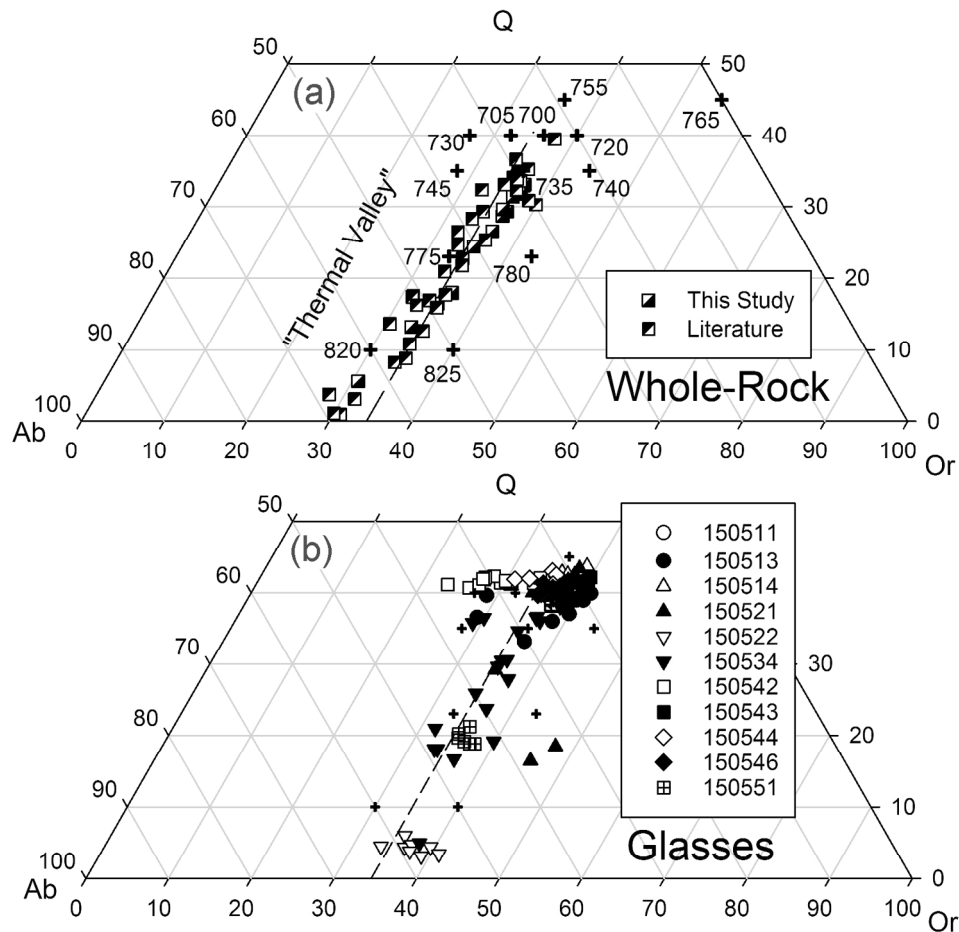


Figure 12. (a) Whole-rock and (b) glass analyses plotted in the system Q-Ab-Or-H<sub>2</sub>O with 8.3 mol% aegirine + 8.3 mol% sodium metasilicate added and PH<sub>2</sub>O = 1000 bar. (Carmichael & MacKenzie, 1963). Whole rock analyses displayed include those presented in this study (Table 2) and from the literature (Civetta et al., 1984, 1989; Kovalenko et al., 1994; Esperança & Crisci, 1995; Avanzinelli et al., 2004; Ferla & Meli, 2006; White et al., 2009; Williams et al., 2014). The crosses mark the alkali feldspar liquidus surface.

153x157mm (300 x 300 DPI)

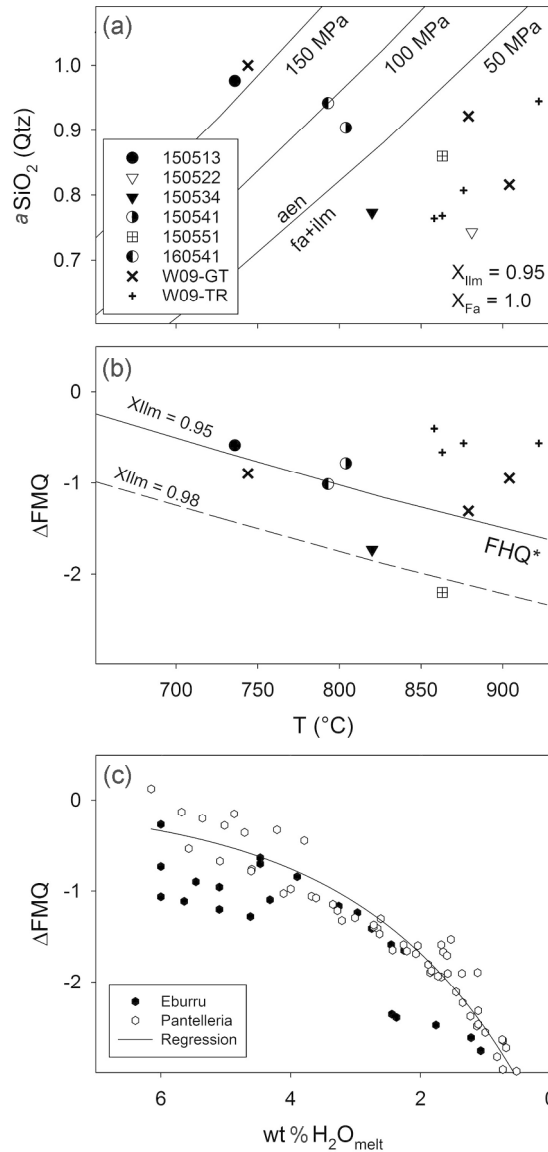


Figure 13. (a) Silica activity ( $a_{\text{SiO}_2}$ ) relative to quartz saturation and (b) oxygen fugacity relative to the FMQ buffer plotted against temperature. W09-GT and W09-TR are the results of QUILF95 geothermobarometry for the Green Tuff and Montagna Grande Trachyte, respectively, from White et al. (2009). The fayalite-ilmenite-aenigmatite stability curve for  $X_{\text{ilm}} = 0.95$  is calculated following Macdonald et al. (2011), with ilmenite activities calculated with the solution model of Andersen & Lindsley (1988).  $\Delta\text{FMQ} = \log f_{\text{O}_2} - \text{FMQ}(T)$ , with  $\text{FMQ}(T)$  calculated following Frost et al. (1988). (c) The experimental results of Scaillet & Macdonald (2006) for Eburru and Di Carlo et al. (2010) for Pantelleria show the strong positive correlation between oxygen fugacity (as  $\Delta\text{FMQ}$ ) and melt water content (wt %  $\text{H}_2\text{O}_{\text{melt}}$ ).

127x267mm (300 x 300 DPI)

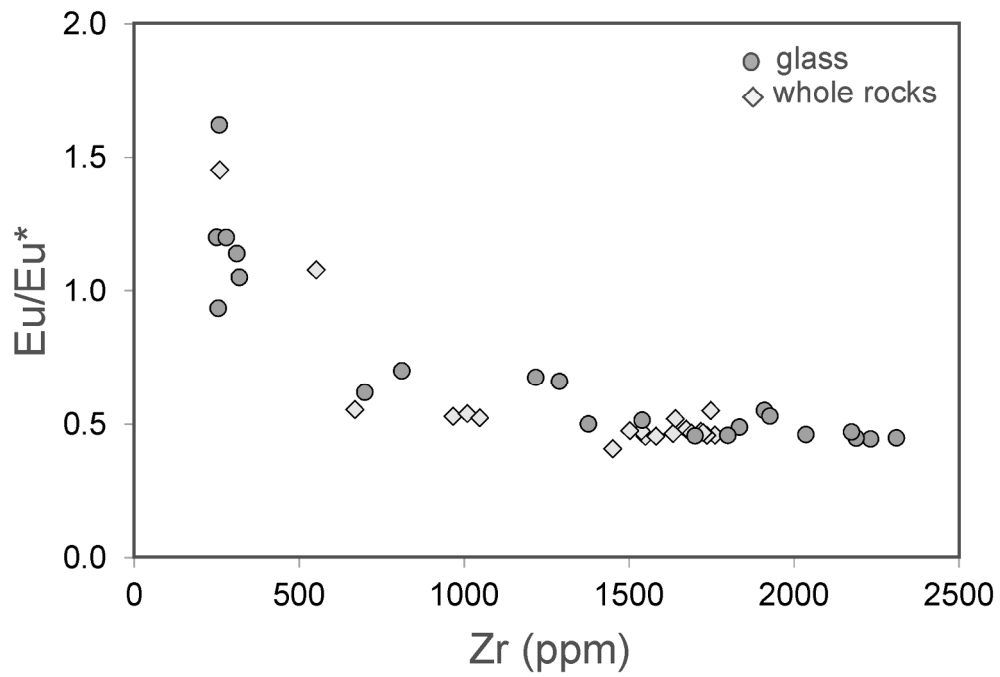


Figure 14.  $\text{Eu}/\text{Eu}^*$  plotted against Zr content for Green Tuff samples. Data sources: whole-rocks – this paper, Table 2; Mahood & Stimac (1990); White et al. (2009); glass – Mahood & Stimac (1990, samples 7, 226, 231/233), Neave et al. (2012, sample 09PNL033), Williams et al. (2014, samples 44H and 44I).

181x122mm (300 x 300 DPI)

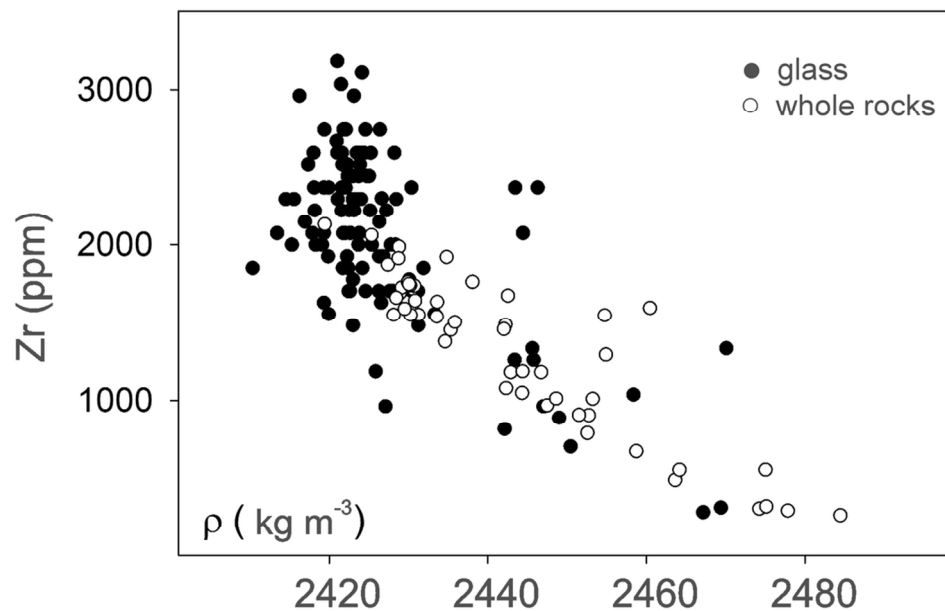


Figure 15. Anhydrous melt densities, calculated by the method of Bottinga & Weill (1970), plotted against Zr contents for whole-rocks (open circles) and glasses (closed circles). The densities initially decrease to Zr  $\sim$ 1500 ppm and then change little with increasing Zr. Data sources: this paper, Table 2 and Electronic Appendix 3.

101x63mm (300 x 300 DPI)

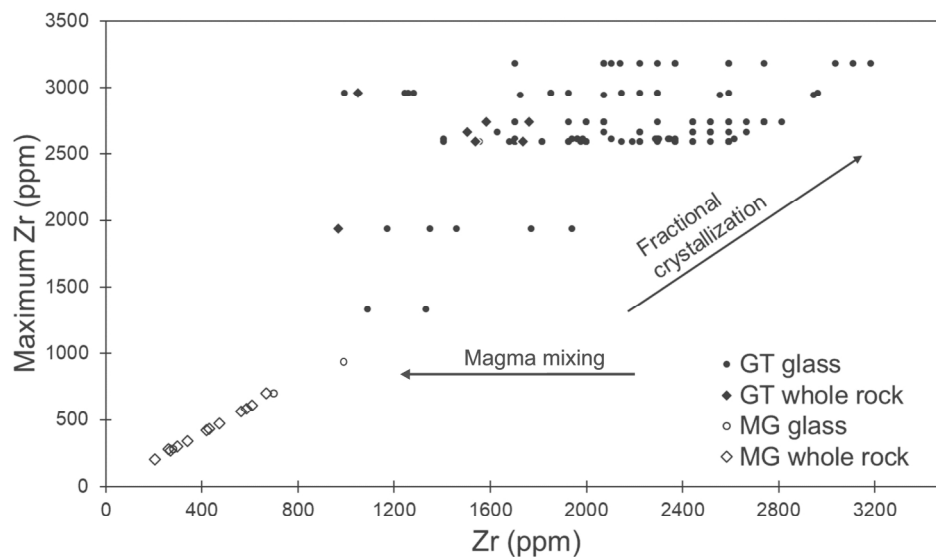


Figure 16. Maximum Zr content in glass in each Green Tuff whole-rock plotted against range of Zr contents in glass of same rock. The ranges indicate mixing in varying proportions of trachytic and rhyolitic melts. Also shown is the composition of a Montagna Grande glass, from Mahood & Stimag (1990, sample 119); its relative compositional similarity to the Montagna Grande whole-rocks suggests that the range of glasses in each sample must be small. Montagna Grande whole-rock data from Mahood & Stimag (1990), Avanzinelli et al. (2004), Ferla & Meli (2006) and White et al. (2009).

180x113mm (300 x 300 DPI)

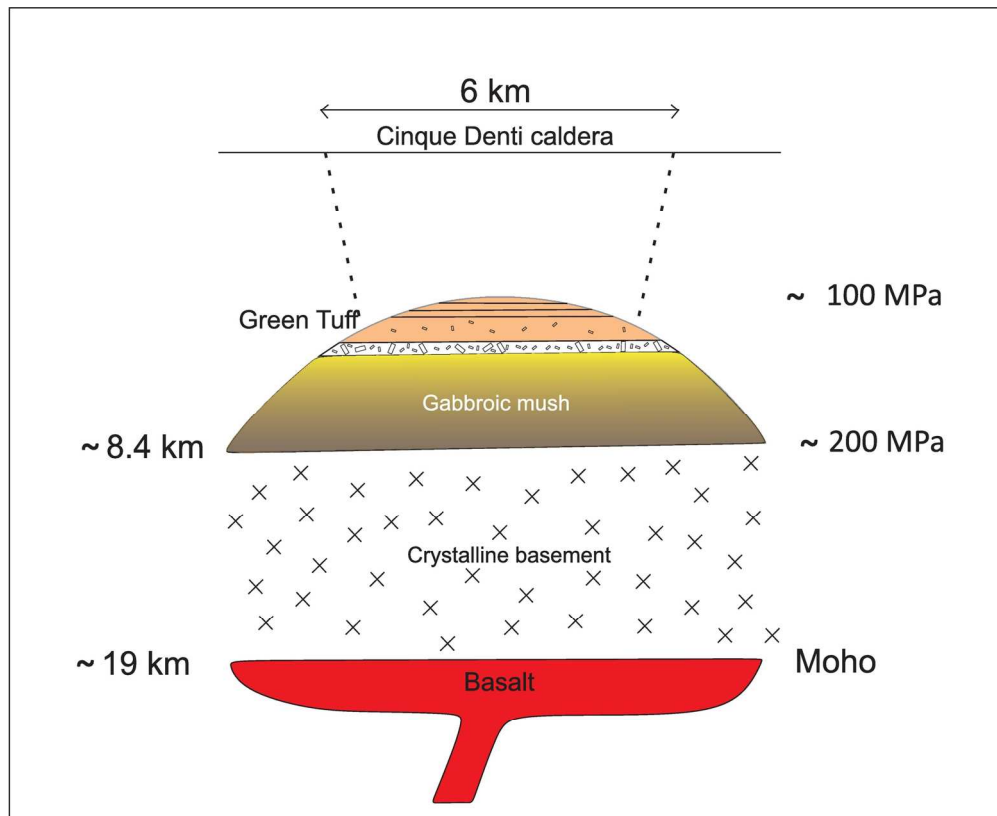


Figure 17. Possible relationships in the magmatic plumbing system prior to eruption of the Green Tuff. The crustal structure is from Civile et al. (1988).

157x128mm (300 x 300 DPI)

## Appendix. Details of analyzed samples

Sample ID	Rock type	Geographic Coordinates		UTM (Zone 32S)	
		Lat (°N)	Long (°E)	mE	mN
150511	eutaxitic lapilli tuff	36.76836	11.96072	764264	4073266
150513	rheomorphic tuff	36.76811	11.95942	764147	4073234
150514	eutaxitic lapilli tuff	36.77172	11.95600	763831	4073626
150521	glassy eutaxitic tuff	36.77378	11.97467	765489	4073904
150522	top of deposit	36.76689	11.98311	766269	4073164
150534	glassy top of section	36.78792	11.94808	763069	4075401
150541	fall deposit (?)	36.81133	11.97583	765465	4078078
150542	lower pumice	36.81992	11.99858	767465	4079092
150543	fiamme bed	36.81986	11.99817	767427	4079085
150544	basal bomb bed	36.82425	11.98381	766133	4079530
150546	vitrophyric base	36.82456	11.98522	766257	4079570
150551	glassy base of deposit	36.83511	11.96942	764811	4080699
160541	densely welded tuff	36.77375	11.97465	765489	4073902
160542	glassy upper unit	36.77423	11.97454	765477	4073955
160543	eutaxitic lapilli tuff	36.77479	11.97427	765451	4074017

Datum for all coordinates is WGS84.

---

Location

---

Punta Tre Pietre

Punta Tre Pietre

Punta Tre Pietre

Monastero Scarp

Monastero Scarp

Contrada Scirafi

Zinedi Scarp

Cinque Denti Scarp

Cinque Denti Scarp

Khartibucale Scarp

Khartibucale Scarp

Punta della Guarda

Monastero Scarp

Monastero Scarp

Monastero Scarp

---

For Peer Review

Table 1. Phenocryst and glass compositions

Sample	Whole rock	Phenocryst compositions							Glass compositions		
		alk feldspar Or%	olivine Fo%	clinopyrox. En%	aenigmat. Ca + Al	ilmenite $X_{ilm}$	magnetite	quartz	apatite REE + Si	ranges SiO <sub>2</sub> wt %	ZrO <sub>2</sub> wt %
150511	p	33.5-36.3	-	7.8-9.4	0.19-0.23	-	-	-	-	69.8-71.0	0.23-0.37
150513	p	23.2-36.6	6.2-9.3	8.4-12.2	-	94.7-95.4	46.7-49.0	-	0.17	67.9-71.3	0.23-0.35
150514	p	26.6-36.2	-	8.1-12.6	0.18-0.23	96.8-98.3	-	+	+	70.0-72.7	0.23-0.40
150521	p	34.6-37.8	-	8.2-10.4	0.16-0.21	-	-	-	+	64.8-73.7	0.23-0.35
150522	ct	19.1-35.4	+	26.1-28.8	-	+	-	+	0.06	60.0-64.9	bd-0.18
150534	p	31.1-36.5	9.5-13.5	8.8-13.3	0.15-0.20	96.3-96.8	70.0-76.0	-	+	64.8-72.9	0.12-0.37
150541	ct	20.1-33.1	15.1-15.8	12.8-21.7	-	+	66.5-73.5	+	0.10-0.24	-	-
150542	p	+	-	+	+	+	-	-	-	69.6-72.1	0.23-0.38
150543	p	+	-	+	+	+	-	-	-	70.1-71.7	0.21-0.35
150544	p	33.0-36.9	-	8.2-11.5	0.16-0.18	+	-	-	+	70.0-73.5	0.23-0.43
150546	p	33.9-35.9	-	8.8-11.2	0.26-0.27	+	-	-	+	69.8-72.7	0.22-0.36
150551	p	29.4-35.9	7.0-12.8	12.3-22.2	0.26-0.27	97.6-98.6	-	-	+	66.7-71.1	bd-0.40
160541	p	33.4-35.5	9.3	43.1-49.6	0.16-0.22	95.6-96.9	-	-	0.16-0.24	-	-
160543	p	34.9-35.7	-	+	+	-	-	?	+	-	-

p, pantellerite; ct, comenditic trachyte (classification scheme of Macdonald (1974)); +, present but not analyzed.

Table 2. Whole-rock compositions of Green Tuff, Pantelleria

Sample	150511	150513	150514	150521	150522	150534	150541	150542	150543	150544	150546	150551	160541	160542	160543	090531	090533
Rock (L)	R	T	T	R	T	T	T	T	T	T	T	T	R	R	R	R	R
Rock (M)	P	P	P	P	CT	P	C	P	P	P	P	P	P	P	P	P	P
wt%																	
SiO <sub>2</sub>	69.22	68.78	67.51	69.07	64.68	65.59	67.34	67.55	68.84	67.99	68.07	67.02	69.51	69.33	69.37	70.16	69.19
TiO <sub>2</sub>	0.50	0.52	0.51	0.50	0.69	0.59	0.47	0.51	0.54	0.51	0.53	0.54	0.48	0.50	0.50	0.53	0.54
Al <sub>2</sub> O <sub>3</sub>	9.27	9.71	9.38	9.39	15.21	12.14	13.88	8.90	9.14	9.69	10.19	12.08	11.39	9.05	9.10	8.95	9.29
FeO*	7.74	7.68	7.46	7.51	5.29	6.87	4.88	7.61	8.06	7.67	7.55	6.61	6.39	7.73	7.74	8.68	9.01
MnO	0.29	0.29	0.28	0.28	0.21	0.26	0.22	0.29	0.30	0.29	0.28	0.26	0.25	0.29	0.29	0.29	0.30
MgO	0.13	0.19	1.36	0.12	0.47	0.27	0.23	0.21	0.14	0.16	0.14	0.17	0.25	0.11	0.12	0.22	0.20
CaO	0.42	0.46	0.52	0.41	1.23	0.66	0.67	0.42	0.43	0.43	0.47	0.62	0.44	0.39	0.42	0.48	0.49
Na <sub>2</sub> O	6.42	6.29	4.97	6.25	6.31	6.09	5.90	5.39	6.34	6.43	6.39	6.42	5.08	6.51	6.03	5.46	5.09
K <sub>2</sub> O	4.60	4.68	4.46	4.62	4.57	4.68	4.92	4.56	4.62	4.60	4.67	4.88	4.91	4.62	4.58	4.50	4.63
P <sub>2</sub> O <sub>5</sub>	0.03	0.03	0.04	0.03	0.15	0.04	0.05	0.04	0.03	0.03	0.03	0.03	0.03	0.03	0.03	0.07	0.03
F	0.12	0.11				0.08	0.08	0.12	0.18		0.13	0.09				0.05	0.08
LOI	0.10	0.10	2.20	0.50	0.20	1.80	0.60	3.20	0.20	0.90	0.40	0.30	0.20	0.10	0.50	-0.10	0.04
Sum	98.84	98.84	98.69	98.68	99.01	99.07	99.24	98.80	98.82	98.70	98.85	99.02	98.93	98.66	98.68	99.29	98.89
O = F	0.05	0.05				0.03	0.03	0.05	0.08		0.05	0.04				0.02	0.03
Total	98.79	98.79	98.69	98.68	99.01	99.03	99.20	98.75	98.75	98.70	98.79	98.99	98.93	98.66	98.68	99.27	98.86
Total C	0.03	0.02	0.05	0.04	0.07	0.03	0.05	0.10	0.02	0.05	0.03	0.03	0.03	0.05	0.04		
Total S	0.03	0.04	0.04	0.03	bd	0.02	<0.02	<0.02	0.03	0.04	0.03	0.03	bd	0.03	0.03	0.01	0.01
ppm																	
Ba	60	80	61	64	1893	153	380	61	52	73	86	148	16	52	62	74	71
Be	4	11	10	13	2	3	4	18	9	8	11	5	6	8	8	12	9
Co	0.5	0.3	0.5	0.2	1.7	0.5	0.4	0.4	0.3	0.3	0.6	0.5	0.3	0.2	0.5	< 0.1	< 0.1
Cs	1.5	1.6	0.2	2	0.2	1.2	0.2	2.5	2.0	1.9	1.8	1.1	0.3	1.8	2.1	1.1	< 0.2
Ga	30.8	32.0	34.9	33.2	31.3	34.1	32.9	30.8	32.6	32.8	34.6	37.1	33.9	34.7	33.6		
Hf	36.8	34.9	38.9	39.1	13	20.8	21.5	39.6	37.8	39	33.9	24.1	34.4	41.0	39.6	39.1	39.8
Nb	286	283.1	310.3	314.2	112.1	196.3	185	313.1	315.9	296.8	274.8	206.2	265.5	315.1	306.9		
Rb	151.1	143.9	114.1	170.7	66	100.6	93.6	160.1	160.8	157.9	142.1	110.8	145.8	170.7	166.0	180	160
Sc	3	3	3	4	10	6	4	3	3	3	4	5	6	3	3	4.1	4.4
Sn	24	12	16	12	8	19	7	12	16	13	12	15	8.0	12.0	12		
Sr	3.3	4.7	29.2	4.3	65.4	8.1	21.7	8.3	3.3	7.7	5.1	6.0	2.4	2.8	4.3	10	8
Ta	17.0	16.5	18.3	18.3	6.5	11.4	10.5	19.0	18.5	19.5	16.7	12.2	17.3	19.9	18.8	20.4	21.8
Th	28.1	27.6	30.1	31.5	10.8	17.4	17.0	31.5	30.0	30.4	26.7	18.4	27.4	32.3	31.3	34.8	32.2
U	8.7	8.8	3.1	9.8	1.3	4.7	1.4	9.6	9.3	9.4	7.8	5.4	5.2	10.2	9.3	7.7	4.5
W	4.1	4.5	1.6	4.5	1.3	2.6	1.4	4.7	4.5	4	3.8	2.8	1.1	5.0	4.9	<1	8
Zr	1582.2	1537.9	1673.8	1718.1	552.5	967.5	1010	1760.6	1736.3	1633.7	1502.9	1047.7	1451.3	1725.2	1689.9	1589.0	1740.0
Y	141.6	136.0	144.3	147.1	50.5	85.0	64.7	161.7	146.5	136.3	130.3	94.0	53.1	146.9	140.0	129.0	100.0
La	188.1	184.7	207.8	203.2	84	116.6	127.3	213.8	207.3	191.8	174.5	135.1	146.6	212.2	204.7	206.0	202.0
Ce	352.2	344.9	377.6	383.3	152.4	214.5	198.5	376.0	375.8	373.2	324.9	244.1	269.7	394.8	394.9	309.0	318.0
Pr	41.91	38.45	40.76	41.57	17.97	25.73	26.81	43.46	41.62	39.43	36.85	28.12	26.94	42.05	41.32		
Nd	143.0	138.5	145.8	147.4	67.3	93.7	100.6	159.4	151.1	138.7	132.1	103.2	92.2	153.7	146.2	135.0	138.0
Sm	27.72	26.86	28.48	28.76	12.68	18.52	17.76	31.22	29.93	27.11	26.38	20.31	14.94	29.24	28.63	23.90	23.60
Eu	4.14	4.20	4.46	4.41	4.38	3.16	3.02	4.71	4.51	4.1	4.13	3.46	1.82	4.45	4.33	4.34	4.35
Gd	25.96	25.17	26.42	26.55	11.74	16.81	15.17	29.4	27.76	24.94	24.54	18.82	11.65	26.92	25.87		
Tb	4.44	4.32	4.42	4.40	1.83	2.81	2.52	5.00	4.74	4.21	4.22	3.11	1.81	4.52	4.40	3.30	3.40
Dy	25.72	25.91	26.36	27.04	10.29	16.42	14.19	29.41	28.27	25.73	24.57	18.28	10.70	26.99	26.89		
Ho	5.14	4.97	5.46	5.64	2.03	3.12	2.55	5.79	5.51	5.21	4.68	3.52	2.03	5.60	5.39		
Er	15.65	15.03	15.25	15.92	5.31	9.34	7.36	17.84	17.05	15.08	14.36	10.54	6.46	15.99	15.61		
Tm	2.21	2.16	2.28	2.28	0.78	1.35	1.08	2.59	2.36	2.18	2.06	1.46	1.02	2.27	2.28		
Yb	13.80	13.97	14.57	14.29	4.92	8.99	7.70	16.08	15.00	13.70	13.46	9.87	7.38	14.93	14.55	13.30	12.00
Lu	2.07	1.98	2.10	2.10	0.68	1.27	1.11	2.33	2.26	2.01	1.94	1.43	1.18	2.18	2.09	1.95	1.78
Peralk Ix	1.68	1.59	1.39	1.63	1.01	1.24	1.08	1.55	1.69	1.61	1.53	1.31	1.20	1.74	1.63	1.55	1.44
Eu/Eu*	0.45	0.47	0.48	0.47	1.08	0.53	0.54	0.46	0.46	0.47	0.47	0.52	0.41	0.47	0.47	0.56	0.57
[La/Yb]	9.78	9.48	10.23	10.20	12.25	9.30	11.86	9.54	9.91	10.04	9.30	9.82	14.25	10.19	10.09	10.44	11.35
[Tb/Yb]	1.46	1.41	1.38	1.40	1.69	1.42	1.49	1.41	1.44	1.40	1.43	1.43	1.11	1.38	1.37	1.09	1.25

p, pantellerite, c, comendite, ct, comenditic trachyte (classification scheme of Macdonald, 1974). T, trachyte, r, rhyolite (TAS scheme, Le Maitre, 2002). Peralk Ix, Peralkalinity Index (mol. (Na<sub>2</sub>O+K<sub>2</sub>O)/Al<sub>2</sub>O<sub>3</sub>). LOI, loss on ignition. Blanks, not deter

Table 3. Representative compositions of matrix glasses and melt inclusions in Green Tuff

	1	2	3	4	5	6	7	8	9	10	11	12
wt%												
SiO <sub>2</sub>	69.96	62.84	63.04	64.79	71.49	67.27	71.90	70.98	66.72	70.68	72.52	72.74
TiO <sub>2</sub>	0.46	1.07	0.72	0.40	0.48	0.47	0.42	0.49	0.69	0.52	0.73	0.72
ZrO <sub>2</sub>	0.27	bd	bd	bd	bd	0.12	0.33	0.43	0.11	0.25	0.40	0.28
Al <sub>2</sub> O <sub>3</sub>	7.86	14.10	14.64	15.16	9.72	11.15	8.05	7.63	11.68	7.87	5.31	5.45
FeO*	8.30	7.02	5.89	4.33	5.39	7.37	7.75	8.05	7.40	7.65	9.93	9.66
MnO	0.32	0.19	0.17	0.14	0.15	0.15	0.42	0.31	0.27	0.31	0.45	0.31
MgO	0.09	0.44	0.35	0.72	0.72	0.23	0.12	0.09	0.16	0.11	0.13	0.15
CaO	0.34	1.74	1.24	0.68	0.80	1.63	0.27	0.26	0.42	0.37	0.46	0.36
Na <sub>2</sub> O	6.26	7.00	6.86	6.68	6.06	6.20	5.84	6.38	6.55	6.11	5.60	5.64
K <sub>2</sub> O	4.58	4.56	5.24	5.58	3.14	4.14	3.41	4.53	4.92	4.55	4.29	4.27
P <sub>2</sub> O <sub>5</sub>	bd	0.26	0.11	bd	bd	bd	bd	bd	bd	bd	bd	bd
Cl	0.93	0.07	bd	0.07	0.07	0.34	1.16	0.99	0.52	0.86	1.05	0.99
SO <sub>3</sub>	0.06	0.07	0.08	0.04	0.06	0.07	0.07	0.10	0.09	0.08	0.16	0.11
Sum	99.43	99.36	98.34	98.59	98.08	99.14	99.74	100.24	99.53	99.36	101.44	101.43
O = Cl	0.21	0.02	0.00	0.02	0.02	0.08	0.27	0.23	0.12	0.20	0.24	0.23
Sum	99.22	99.34	98.34	98.57	98.06	99.06	99.47	100.01	99.41	99.16	101.20	101.20
P.I.	1.94	1.17	1.16	1.12	1.38	1.32	1.65	2.02	1.38	1.90	2.61	2.55

Explanation: 1, pale brown glass, sample 150511; 2, dark bleb, 150522; 3, melt inclusion in feldspar, 150522; 4, 5, black blebs of glass, 150534;

6, pale glass, 150534; 7, brown glass, 150542; 8, grey speckled glass, 150544; 9, 10, brown glass, 150551; 11, 12, melt inclusions in feldspar, 150514.

FeO\*, all Fe as Fe<sup>2+</sup>. bd, below detection. P.I., peralkalinity index (mol. (Na<sub>2</sub>O+K<sub>2</sub>O)/Al<sub>2</sub>O<sub>3</sub>).

For Peer Review

1  
2  
3  
4  
5  
6  
7  
8  
9  
10  
11  
12  
13  
14  
15  
16  
17  
18  
19  
20  
21  
22  
23  
24  
25  
26  
27  
28  
29  
30  
31  
32  
33  
34  
35  
36  
37  
38  
39  
40  
41  
42  
43  
44  
45  
46  
47

Table 4. Results of major-element mass balance modelling.

	Parent	Daughter	Mineral Phases					Calc	r	Results		
(A) Comenditic Trachyte Glass to Pantellerite Glass												
	150522	150514	Anr	Aug	Ol	Ilm	Ap					
SiO <sub>2</sub>	65.07	71.38	67.45	49.07	30.37	0.00	0.00	65.08	-0.01	150514	0.07	= F
TiO <sub>2</sub>	0.71	0.36	0.00	0.21	0.00	52.08	0.00	0.72	-0.01	Anr	0.86	92.5%
Al <sub>2</sub> O <sub>3</sub>	16.05	7.34	18.17	0.44	0.00	0.00	0.00	16.10	-0.04	Aug	0.03	2.8%
FeO*	4.30	9.49	0.76	25.20	60.08	45.73	0.57	4.29	0.01	Ol	0.03	3.0%
MnO	0.17	0.82	0.00	1.46	4.03	1.99	0.20	0.24	-0.07	Ilm	0.01	1.4%
MgO	0.21	0.13	0.00	3.88	4.93	0.20	0.06	0.25	-0.04	Ap	0.00	0.3%
CaO	0.76	0.20	0.07	18.79	0.58	0.00	57.13	0.73	0.03		1.00	
Na <sub>2</sub> O	6.67	5.90	7.49	0.94	0.00	0.00	0.00	6.86	-0.19			
K <sub>2</sub> O	5.97	4.37	6.07	0.00	0.00	0.00	0.00	5.51	0.46			
P <sub>2</sub> O <sub>5</sub>	0.07	0.00	0.00	0.00	0.00	0.00	42.04	0.11	-0.04			
P.I.	1.08	1.96						99.90	0.255	= $\Sigma r^2$		
(B) Comenditic Trachyte Glass to Pantellerite Melt Inclusion												
	150522	150514	Anr	Aug	Ol	Ilm	Ap			150514	0.06	= F
SiO <sub>2</sub>	65.07	72.94	67.45	49.07	30.37	0.00	0.00	65.09	-0.01	Anr	0.87	92.5%
TiO <sub>2</sub>	0.71	0.73	0.00	0.21	0.00	52.08	0.00	0.72	-0.01	Aug	0.02	2.6%
Al <sub>2</sub> O <sub>3</sub>	16.05	5.34	18.17	0.44	0.00	0.00	0.00	16.08	-0.03	Ol	0.03	3.2%
FeO*	4.30	9.99	0.76	25.20	60.08	45.73	0.57	4.29	0.01	Ilm	0.01	1.4%
MnO	0.17	0.45	0.00	1.46	4.03	1.99	0.20	0.21	-0.04	Ap	0.00	0.3%
MgO	0.21	0.13	0.00	3.88	4.93	0.20	0.06	0.25	-0.04		1.00	
CaO	0.76	0.46	0.07	18.79	0.58	0.00	57.13	0.73	0.04			
Na <sub>2</sub> O	6.67	5.63	7.49	0.94	0.00	0.00	0.00	6.86	-0.19			
K <sub>2</sub> O	5.97	4.32	6.07	0.00	0.00	0.00	0.00	5.53	0.44			
P <sub>2</sub> O <sub>5</sub>	0.07	0.00	0.00	0.00	0.00	0.00	42.04	0.12	-0.05			
P.I.	1.08	2.61						Sum:	99.88	0.240	= $\Sigma r^2$	
(C) Pantellerite Glass to Pantellerite Glass (Horizontal Trend)												
	150514	150544	Anr	Cpx	Aen	Qtz				150544	0.92	= F
SiO <sub>2</sub>	71.38	71.90	67.25	49.66	40.35	100.00		71.38	0.00	150544	0.92	= F
TiO <sub>2</sub>	0.36	0.50	0.00	0.39	8.83	0.00		0.81	-0.45	Anr	0.01	6.5%
Al <sub>2</sub> O <sub>3</sub>	7.34	7.73	17.89	0.12	0.50	0.00		7.23	0.11	Cpx	0.01	10.9%
FeO*	9.49	8.15	1.09	26.32	40.56	0.00		9.35	0.15	Aen	0.04	48.3%
MnO	0.82	0.31	0.00	1.50	1.39	0.00		0.36	0.47	Qtz	0.03	34.3%
MgO	0.13	0.09	0.00	3.09	1.09	0.00		0.15	-0.02		1.00	
CaO	0.20	0.26	0.00	17.05	0.55	0.00		0.42	-0.21			
Na <sub>2</sub> O	5.90	6.46	7.52	1.87	6.69	0.00		6.27	-0.37			
K <sub>2</sub> O	4.37	4.59	6.26	0.00	0.02	0.00		4.26	0.11			
P <sub>2</sub> O <sub>5</sub>	0.00	0.00	0.00	0.00	0.00	0.00		0.00	0.00			
P.I.	1.96	2.02						Sum:	100.23	0.654	= $\Sigma r^2$	

Minerals: Anr, Anorthoclase; Cpx, clinopyroxene; Ol, olivine; Ilm, ilmenite; Ap, apatite; Aen, aenigmatite; Qtz, quartz.

Model results: F, liquid proportion;  $\Sigma r^2$ , sum of the squares of the residuals. Apatite and aenigmatite compositions adapted from White *et al.* (2009).

P.I., Peralkalinity Index (mol. (Na<sub>2</sub>O+K<sub>2</sub>O)/Al<sub>2</sub>O<sub>3</sub>)

Table 5. Results of geothermometry and oxygen barometry calculated with QUILF95 (Andersen *et al.*, 1993)

Sample		Ilmenite			Spinel			Olivine		Augite		aSiO <sub>2</sub> (Q)	T (°C)	log <i>f</i> O <sub>2</sub>	ΔFMQ
		X-Hem	X-Gk	X-Py	N-Ti	N-Mg	N-Mn	X-Fo	X-La	X-En	X-Wo				
160541	Input	0.042	<i>0.013</i>	<i>0.047</i>				0.079	<i>0.008</i>	0.125	0.428				
	Calc		0.012						0.008			0.942	793	-15.7	-1.01
150513	Input	0.047	<i>0.024</i>	<i>0.056</i>				0.069	0.006	<i>0.112</i>	0.435				
	Calc		0.009							0.121		0.976	736	-16.6	-0.58
150522	Input	+						0.251	0.009	<i>0.283</i>	0.270				
	Calc									0.270		0.743	881		
150534	Input	0.035	<i>0.016</i>	<i>0.044</i>	0.723	<i>0.017</i>	0.053			0.101	0.424				
	Calc		0.010	0.032		0.012						0.773	820	-15.8	-1.73
150541	Input	+			0.667	<i>0.021</i>	0.055	0.153	0.007	<i>0.195</i>	0.419				
	Calc					0.026				0.207		0.904	804	-15.2	-0.78
150551	Input	0.013	<i>0.008</i>	<i>0.042</i>				0.126	0.011	<i>0.138</i>	0.423				
	Calc		0.021							0.170		0.860	863	-15.4	-2.20
231	Input				0.719	<i>0.042</i>	0.057	0.262	0.009	<i>0.296</i>	0.410				
	Calc					0.058				0.275		0.816	904	-13.4	-0.95
226	Input				0.763	<i>0.039</i>	0.056	0.140	0.010	<i>0.203</i>	0.405				
	Calc					0.029				0.181		0.922	879	-14.2	-1.31
060537	Input	0.039	<i>0.009</i>	<i>0.050</i>				0.058	0.006	<i>0.113</i>	<i>0.422</i>	1.000			
	Calc		0.008							0.103	0.427		744	-16.7	-0.89

All results are calculated at P = 100 MPa. Entries in italics in the "Input" row signify values that were set as trial values; the values calculated by QUILF95 are in normal font in the "Calc" row. Silica activity is relative to quartz saturation. ΔFMQ = log *f*O<sub>2</sub> - FMQ(T). Samples 231 and 226 are from mineral analyses reported by Mahood & Stimac (1990); sample 060537 is from mineral analyses reported by White *et al.* (2009). +, present but not analyzed.